

## Electronic Supplementary Information

### Hydroxy-bridged Resting States of a [NiFe]-Hydrogenase Unraveled by Cryogenic Vibrational Spectroscopy and DFT Computations

Giorgio Caserta,<sup>a,†\*</sup> Vladimir Pelmeshnikov,<sup>a,†\*</sup> Christian Lorent,<sup>a</sup> Armel F. Tadjoung Waffo,<sup>a</sup> Sagie Katz,<sup>a</sup> Lars Lauterbach,<sup>a</sup> Janna Schoknecht,<sup>a</sup> Hongxin Wang,<sup>b</sup> Yoshitaka Yoda,<sup>c</sup> Kenji Tamasaku,<sup>d</sup> Martin Kaupp,<sup>a</sup> Peter Hildebrandt,<sup>a</sup> Oliver Lenz,<sup>a</sup> Stephen P. Cramer,<sup>b\*</sup> and Ingo Zebger<sup>a\*</sup>

<sup>a</sup> *Institut für Chemie, Technische Universität Berlin, Straße des 17. Juni 135, 10623 Berlin, Germany*

<sup>b</sup> *SETI Institute, 189 Bernardo Avenue, Mountain View, CA 94043, United States*

<sup>c</sup> *Japan Synchrotron Radiation Research Institute (JASRI), SPring-8, 1-1-1 Kouto, Sayo-gun, Hyogo 679-5198, Japan*

<sup>d</sup> *RIKEN SPring-8 Center, 1-1-1 Kouto, Sayo-cho, Sayo-gun, Hyogo 679-5148, Japan*

\*corresponding authors

† These authors contributed equally

### Table of Contents

#### Materials and Methods

- **Protein purification** (page S3).
- **NRVS sample preparation** (page S3).
- **Infrared spectroscopy** (pages S3-S4).
- **Electron paramagnetic resonance spectroscopy** (page S4).
- **Nuclear resonance vibrational spectroscopy** (pages S4-S5).
- **DFT calculations** (pages S5-S6).

#### Supplementary Results

- **NRVS characterization of the regulatory [NiFe]-hydrogenase** (page S6).
- **Extended DFT analysis of the NRVS-relevant vibrational modes** (pages S7-S9).

#### Supplementary Figures: S1-S20

**Fig. S1** IR spectra of as-isolated RH recorded at 283 K and at different pH values showing the absorptions related to  $\nu(\text{CO})$  and  $\nu(\text{CN})$  stretching modes of the active site (page S9).

**Fig. S2** IR spectra of as-isolated HoxC (HoxC<sub>ai</sub>) at different temperatures (page S10).

**Fig. S3** EPR spectra of HoxC<sub>ai</sub> and chemically oxidized HoxC<sub>ox</sub> measured at 20 K (page S11).

**Fig. S4** Homology model of the HoxC active site and its adjacent protein environment, which was used for the DFT calculations (page S12).

**Fig. S5** Best-fitting DFT-optimized HoxC models for the Ni<sub>r</sub>-S<sub>I</sub> (model Ni<sub>r</sub>-S<sub>μOH</sub><sup>SH</sup>, red) and Ni<sub>r</sub>-B'' (model Ni<sub>r</sub>-B<sub>μOH</sub><sup>SH</sup>, blue) states, both containing a bridging μOH<sup>-</sup> ligand and a protonated Ni-bound Cys479 cysteine (page S13).

**Fig. S6** DFT-optimized models of the Ni<sub>r</sub>-S resting state containing a bridging μOH<sup>-</sup> ligand and either protonated (best-fit model Ni<sub>r</sub>-S<sub>μOH</sub><sup>SH</sup>) or deprotonated (alternative model Ni<sub>r</sub>-S<sub>μOH</sub><sup>S<sup>-</sup></sup>) Cys479. A second alternative model contained Cys60 in its protonated form (alternative model Ni<sub>r</sub>-S<sub>μOH</sub><sup>Cys60-SH</sup>) (page S14).

**Fig. S7** DFT-optimized models of the Ni<sub>r</sub>-B resting state containing a bridging μOH<sup>-</sup> ligand and either protonated (best-fitting model Ni<sub>r</sub>-B<sub>μOH</sub><sup>SH</sup>) or deprotonated (alternative model Ni<sub>r</sub>-B<sub>μOH</sub><sup>S<sup>-</sup></sup>) Cys479 (page S15).

**Fig. S8** Alternative DFT-optimized models of the Ni<sub>r</sub>-S state containing a bridging μH<sub>2</sub>O ligand and either deprotonated (model Ni<sub>r</sub>-S<sub>μH<sub>2</sub>O</sub><sup>S<sup>-</sup></sup>) or protonated (model Ni<sub>r</sub>-S<sub>μH<sub>2</sub>O</sub><sup>SH</sup>) Cys479 (page S16).

**Fig. S9** Alternative DFT-optimized models for the HoxC<sub>ai</sub> active site in the Ni<sub>r</sub>-S<sub>I</sub> state containing an Fe-bound terminal H<sub>2</sub>O ligand and either a deprotonated (Ni<sub>r</sub>-S<sub>Fe-H<sub>2</sub>O</sub><sup>S<sup>-</sup></sup>) or a protonated (Ni<sub>r</sub>-S<sub>Fe-H<sub>2</sub>O</sub><sup>SH</sup>) terminal cysteine Cys479 (page S17).

**Fig. S10** Alternative DFT-optimized models of the Ni<sub>r</sub>-S state containing a terminal H<sub>2</sub>O ligand and either deprotonated (model Ni<sub>r</sub>-S<sub>Ni-H<sub>2</sub>O</sub><sup>S<sup>-</sup></sup>) or protonated (model Ni<sub>r</sub>-S<sub>Ni-H<sub>2</sub>O</sub><sup>SH</sup>) Cys479 (page S18).

**Fig. S11** Experimental low-temperature and DFT-computed IR spectra displaying bands related to the CO and CN<sup>-</sup> ligands of the active site in the HoxC<sub>ai</sub> and HoxC<sub>ox</sub> proteins (page S19).

**Fig. S12** Low-temperature IR spectra of HoxC<sub>ai</sub> residing in the Ni<sub>r</sub>-S<sub>I</sub> and Ni<sub>r</sub>-S<sub>II</sub> resting states in comparison to DFT-predicted infrared bands using different Ni<sub>r</sub>-S models of the active site (page S20).

**Fig. S13** NRVS data recorded on the [<sup>57</sup>Fe]-enriched DvMF [NiFe]-hydrogenase in the Ni<sub>u</sub>-A state and [<sup>57</sup>Fe]-enriched RH in the Ni<sub>a</sub>-S state (page S21).

**Fig. S14** NRV spectra of <sup>57</sup>Fe-enriched RH and HoxC (page S22).

**Fig. S15** Experimental NRV spectrum of <sup>57</sup>Fe-enriched HoxC<sub>ox</sub> protein (page S23).

**Fig. S16** Comparison of the experimental NRV spectrum of HoxC<sub>ai</sub> with computed spectra derived from different active site models (page S24).

**Fig. S17** Comparison of the experimental NRV spectrum of HoxC<sub>ox</sub> with computed spectra derived from different active site models (page S25).

**Fig. S18** Overlay of the experimental NRV spectra for HoxC<sub>ai</sub> and HoxC<sub>ox</sub> and those derived from the corresponding DFT calculations (page S26).

**Fig. S19** Analysis of the computed <sup>57</sup>Fe-PVDOS (NRVS) spectra (page S27).

**Fig. S20** NRV spectra of HoxC<sub>ai</sub> (Ni<sub>r</sub>-S<sub>i</sub>), HoxC<sub>ox</sub> (Ni<sub>r</sub>-B'') and native RH (Ni<sub>a</sub>-S) including error bars (page S28).

**Supplementary References** (page S29).

## Materials and Methods

**Protein purification.** *R. eutropha* strains for RH and HoxC overproduction have been previously described.<sup>1,2</sup> *R. eutropha* precultures were grown for 48 h at 30 °C and 120 rpm in mineral medium composed of H16 buffer (25 mM Na<sub>2</sub>HPO<sub>4</sub>, 11 mM KH<sub>2</sub>PO<sub>4</sub>, pH 7.0) supplemented with mineral salts (37.5 mM NH<sub>4</sub>Cl, 1 μM NiCl<sub>2</sub>, 18 μM <sup>57</sup>FeCl<sub>2</sub>, 68 μM CaCl<sub>2</sub> and 810 μM MgSO<sub>4</sub>) and tetracycline (22.5 μM). The carbon end energy source was provided in form of 0.4 % (w/v) fructose. Main cultures were grown in the same medium except that 0.05% fructose and 0.4 % glycerol were provided as carbon and energy source. Cultivation took place in Erlenmeyer flasks (filled to 80% of their capacity) at 30 °C and 120 rpm until the optical density at 436 nm reached a value of 11-13. Cells were harvested by centrifugation (11500 x g, 277 K, 25 min), flash frozen in liquid nitrogen and stored at 200 K until further use. RH and HoxC were purified as described earlier.<sup>2,3</sup>

**NRVS sample preparation.** Freshly purified, [<sup>57</sup>Fe]-enriched HoxC<sub>ai</sub> was concentrated to 1.3 mM. A volume of 30-35 μl was filled into a Kapton tape-sealed NRVS-cell, flash frozen and stored in liquid nitrogen until the measurement. A second aliquot (1.3 mM HoxC, 35 μl) was treated with 3 molar equivalents of K<sub>3</sub>Fe(CN)<sub>6</sub> as described previously,<sup>2</sup> yielding [<sup>57</sup>Fe]-enriched HoxC<sub>ox</sub>. [<sup>57</sup>Fe]-enriched RH was purified as described previously,<sup>1,3</sup> lyophilized and concentrated prior to the NRVS measurements. The protein powder was filled into a Kapton tape-sealed NRVS cell, flash frozen and stored in liquid nitrogen until the measurement.<sup>4</sup>

**Infrared spectroscopy.** HoxC and RH protein solutions were transferred into a homemade transmission cell with CaF<sub>2</sub> windows with an optical pathlength of 50 μm, provided by a Teflon spacer. Spectra with 2 cm<sup>-1</sup> resolution were recorded at 283 K in a Tensor 27 FTIR spectrometer (Bruker) equipped with a liquid nitrogen-cooled MCT detector by averaging 200 scans. The sample compartment was purged with dry air. A spectrum of buffer (50 mM Tris-HCl 8.0, 150 mM NaCl) was used as a reference to calculate baseline-corrected absorbance spectra. Bruker

OPUS software 7.5 was used for data evaluation. Samples for cryogenic IR measurements were transferred into a gas-tight cryo-IR transmission cell consisting of two CaF<sub>2</sub> windows and a 50- $\mu$ M Teflon spacer. The cell was placed into a homemade liquid nitrogen cryostat, mounted into the sample compartment of a Bruker Tensor 27 FTIR spectrometer equipped with a liquid nitrogen cooled MCT detector. HoxC and RH samples were analyzed in a concentration range of 1.0-1.5 mM and 0.2-0.5 mM, respectively. Samples for cryo-IR measurements were buffer-exchanged with 50 mM Tris-HCl (pH 8.0 at 277 K) containing 150 mM NaCl and 25 % (v/v) glycerol. IR spectra of [<sup>57</sup>Fe]-HoxC and [<sup>57</sup>Fe]-HoxC<sub>ox</sub> were recorded before and after NRVS measurements to ensure that the active site was not affected by the high photon flux of the BL19LXU beamline of SPring-8 (data not shown).

**Electronic Paramagnetic Resonance spectroscopy.** A Bruker EMXplus spectrometer equipped with an ER 4122 SHQE resonator, an Oxford EPR 900 helium flow cryostat and an Oxford ITC4 temperature controller was used for the EPR spectroscopic experiments. The baseline correction was performed by subtracting the spectrum of buffer solution from that of the sample, both measured with the same parameters. If necessary, the spectra were additionally corrected using a polynomial or spline function. Experimental parameters: 1 mW microwave power, microwave frequency 9.29 GHz, modulation amplitude 10 G and 100 kHz modulation frequency. Spectra simulation was performed with the Matlab toolbox Easyspin 5.2.25. HoxC<sub>ox</sub> samples were analyzed in a concentration range of c.a. 0.5-1.0 mM (70-100  $\mu$ l).

**Nuclear resonance vibrational spectroscopy.** NRVS measurements were conducted at SPring-8 BL19LXU<sup>5</sup> (with a flux of ca.  $6 \cdot 10^9$  photons  $\cdot$  s<sup>-1</sup>) using 14.4 keV radiation with  $\approx$ 1.0 eV resolution. A high energy resolution monochromator (HRM) [Ge(331) $\times$ 2Si(975)] was employed to increase the resolution to 0.8 meV. The beam size was also  $0.6 \cdot 1$  mm<sup>2</sup>. A 2  $\cdot$  2 avalanche photodiode (APD) detector array was used to collect the delayed nuclear fluorescence and the K $\alpha$  fluorescence following nuclear excitation. Raw NRVS data were converted to single-phonon <sup>57</sup>Fe-PVDOS using the PHOENIX software<sup>6</sup> package through spectratools (<https://www.spectra.tools/>).<sup>7</sup> The energy scales were calibrated with a standard sample of [NEt<sub>4</sub>][<sup>57</sup>FeCl<sub>4</sub>] with a prominent peak at 380 cm<sup>-1</sup>. The sample temperature was maintained at 10 K with a liquid-helium cryostat during acquisition time. The Stoke/anti-Stoke imbalance derived real sample temperatures that were 40-70 K.<sup>8</sup> In order to emphasize the region of interest, sectional measurements of the spectral regions were performed. Each scan was divided into segments with different data collection times (second per point, s/p). We used 3-4 s/p for the range from -220 to 80 cm<sup>-1</sup>, 5-7 s/p from 88 to 420 cm<sup>-1</sup>, 14-18 s/p for the 420-

700 cm<sup>-1</sup> region, containing Fe–CN/CO vibrational modes. The scan ranges are all relative to the resonance energy.

**DFT calculations.** Due to the absence of X-ray structural data for both RH and HoxC, initial coordinates used for the DFT calculations were based on the crystal structure at 1.50 Å resolution of the O<sub>2</sub>-tolerant membrane-bound hydrogenase (MBH) from *R. eutropha* in the Ni-SR state (PDB 3RGW).<sup>9</sup> The DFT model included the [NiFe] core and all the side chains having their non-hydrogen interatomic distances within 4 Å from the 1<sup>st</sup>-shell ligands of the two metal sites. Hydrogen bonds between the protein and the CO/CN<sup>-</sup> ligands were thus explicitly considered. The model contained the conserved Asp117/102 (MBH/RH aligned sequence numbers, respectively) showing an ionic interaction to Arg530/411. For two sub-sequences C75/60-G76/G61-V77/I62-C78/63 and C597/479-L598/M480-A599/V481-C600/482, each of which spanned by two Cys residues coordinating the Ni center, the backbone spacers (replaced with Ala residues) were additionally included. Apart from that, the model was based on the MBH active site and contained three amino acid exchanges, namely His82-to-Gln67, Pro529-to-Ala410, and Val551-to-Ala432, to adopt the HoxC sequence.<sup>10,11</sup> For the two representative active site arrangements, Ni<sub>r</sub>-S<sub>μ</sub>OH<sup>SH</sup> / Ni<sub>r</sub>-B<sub>μ</sub>OH<sup>SH</sup>, calculations were done as well using an alternative minimal ('...MIN') model which included only the four cysteine residues coordinating the [NiFe] core. All the 18×C<sub>α</sub> (4×C<sub>α</sub>) carbon nuclei of the resulting extended (minimal) model were locked to their original X-ray positions during structural optimizations. Single point self-consistent field (SCF) calculations using JAGUAR 9.4<sup>12</sup> were done to receive wavefunction (electron density) solutions for the non-optimized structures. This approach was aided by high-quality initial guess protocol of JAGUAR 9.4 on the wavefunction, employing the ligand field theory for the metal *d*-orbitals. The solutions from JAGUAR 9.4 were then transferred as inputs to GAUSSIAN 09 Revision D.01,<sup>13</sup> used to accomplish structure optimizations and subsequent Hessians. All the calculations employed PBE0<sup>14</sup> hybrid functional and LACV3P\*\* basis set (as implemented in JAGUAR 9.4 and exported to GAUSSIAN 09). For the first- and second-row elements, LACV3P\*\* implies 6-311G\*\* triple-ζ basis sets including polarization functions. For the Fe atoms, LACV3P\*\* consists of a triple-ζ basis set for the outermost core and valence orbitals, and the quasi-relativistic Los Alamos effective core potential (ECP) for the innermost electrons.<sup>15,16</sup> The molecular systems environment was considered using a self-consistent reaction field (SCRF) polarizable continuum model and integral equation formalism (IEF-PCM)<sup>17</sup> as implemented in GAUSSIAN 09. The static dielectric constant set to ε = 4.0, as often used for proteins, and the remaining IEF-PCM parameters were kept at their default values for water. The PVDOS, IR,

and interatomic relative displacement kinetic energy distribution (KED) intensities were extracted from GAUSSIAN 09 normal mode outputs using an in-house program Q-SPECTOR, successfully applied in previous studies.<sup>19–23</sup> To empirically account for the observed NRVS lineshape, the computed <sup>57</sup>Fe-PVDOS intensities were broadened by Lorentzian convolution with a full width at half maximum (FWHM) = 12 cm<sup>-1</sup>. For <sup>57</sup>Fe-PVDOS, empirical scaling by ×0.97 and ×0.96 was applied to the calculated frequencies in the 500-600 cm<sup>-1</sup> and > 600 cm<sup>-1</sup> regions, respectively. For the corresponding IR spectra, the calculated CO/CN band frequencies were fit linearly to the experimental IR band positions corresponding to the Ni<sub>r</sub>-S<sub>I</sub> and Ni<sub>r</sub>-B'' states observed in the 1850-2150 cm<sup>-1</sup> range, producing ×0.864 slope and +173.6 cm<sup>-1</sup> offset parameters.

## Supplementary Results

**NRVS characterization of the regulatory [NiFe]-hydrogenase.** The regulatory [NiFe]-hydrogenase from *Ralstonia eutropha* (RH) harbors three [4Fe4S] clusters in addition to the catalytic center. The NRVS spectrum of RH, as those for all other [NiFe]-hydrogenases, is dominated by the Fe-S vibrational bands originating from the FeS clusters (**Fig. 4**). The spectral features are related to i) torsional modes of the clusters located below 100 cm<sup>-1</sup>, ii) breathing and S-Fe-S bending modes found around 150 cm<sup>-1</sup> and iii) Fe-S stretching vibrations detected in the region between 250 cm<sup>-1</sup> and 420 cm<sup>-1</sup>. Similar NRVS band patterns were previously observed for the [NiFe]-hydrogenase from *Desulfovibrio vulgaris* Miyazaki F (*DvMF*, see also **Fig. S13**).<sup>18</sup> However, small spectral variations are readily visible and probably related to differences in the FeS cluster composition, as the *DvMF* enzyme contains two [4Fe4S] clusters and one [3Fe4S] species. Because of the dominant contribution of the FeS clusters, accounting for 12 of the 13 Fe ions in RH, bands related to the active site were visible exclusively in the high frequency region above 420 cm<sup>-1</sup> (**Fig. 4**). Upon normalization of the HoxC and RH spectra to the total iron content (13 Fe in RH vs. 1 Fe in HoxC) (**Fig. S14a**), the relative intensities of the bands above 500 cm<sup>-1</sup> became directly comparable (**Fig. S14b**). Because of the poor spectral resolution in the 400 – 500 cm<sup>-1</sup> region, caused by both low band intensities and overlapping contributions, several bands could not be properly assigned (highlighted with an asterisk in **Fig. S14b**). Despite these limitations, the NRVS spectra of RH and HoxC confirm that the active sites in both samples reside in different states, which is consistent with the data obtained from the low-temperature IR measurements (**Fig. 2b**).

**Extended DFT analysis of the NRVS-relevant vibrational modes.** As described in the main text of this work, the DFT models  $\text{Ni}_r\text{-S}_{\mu\text{OH}}^{\text{SH}}/\text{Ni}_r\text{-B}_{\mu\text{OH}}^{\text{SH}}$  correspond to the low-temperature IR signatures of the  $\text{HoxC}_{\text{ai}}/\text{HoxC}_{\text{ox}}$  protein samples in the  $\text{Ni}_r\text{-S}_i/\text{Ni}_r\text{-B}''$  states. A spectra-style vibrational analysis of these active site models is provided in **Fig. S19**, which displays the Ni/Fe ligand contributions to the  $^{57}\text{Fe}$ -PVDOS (NRVS) profiles in detail. Animated representations of selected vibrational modes are provided as a separate part of the ESI.

The red shifts of the  $^{57}\text{Fe}$ -PVDOS bands upon oxidation of  $\text{Ni}_r\text{-S}$  to  $\text{Ni}_r\text{-B}$ , which are typically within  $\sim 15\text{ cm}^{-1}$  in magnitude, are very well reproducible in the corresponding DFT calculations of the normal modes. The vibrational energies listed below correspond to the models  $\text{Ni}_r\text{-S}_{\mu\text{OH}}^{\text{SH}}/\text{Ni}_r\text{-B}_{\mu\text{OH}}^{\text{SH}}$ , which differ in charge by one  $e^-$  unit. Prominent modes of a mixed Fe–CO/CN (**Fig. S19e,f**) bending character appear in the high-end region ( $\sim 580\text{--}620\text{ cm}^{-1}$ ) of the spectra at  $615/604\text{ cm}^{-1}$  (mostly Fe–CO bending) and  $591/585\text{ cm}^{-1}$  (mostly Fe–CN bending). The modes at  $551/544\text{ cm}^{-1}$  exhibit the highest individual intensity across the entire spectrum and have predominantly Fe–CO stretching character, with a minor admixture from the Fe/Ni– $\mu\text{OH}$  bending motion. The Fe–CN stretching modes dominate the  $\sim 400\text{--}500\text{ cm}^{-1}$  region of  $^{57}\text{Fe}$ -PVDOS.

The largest magnitude  $\mu\text{OH}^-$  displacements, correlated with the  $\mu\text{O}(\text{H})$ -PVDOS profile (**Fig. S19b**) are attributed to the Ni– $\mu\text{OH}$  stretches at  $506/494\text{ cm}^{-1}$  (**Fig. S19c**), Fe– $\mu\text{OH}$  stretches at  $424/409\text{ cm}^{-1}$  (**Fig. S19d**), and the Ni– $\mu\text{OH}$ –Fe wagging modes at  $284/268\text{ cm}^{-1}$  where the  $\mu\text{OH}^-$  ligand moves perpendicularly to the Ni–Fe axis of the active site. The modes are visualized in the active site model as depicted in **Fig. 7**. Finally, essentially pure  $\mu\text{O}$ –H bending modes involving displacement of the hydroxyl proton were calculated at vibrational energies above  $720\text{ cm}^{-1}$ , associated with very small  $^{57}\text{Fe}$ -PVDOS intensities (**Fig. S18b, S19a**) at the level of the experimental error (**Fig. S20**); the  $\mu\text{O}$ –H bending motions admix as well to the Fe–CO/CN modes in the  $\sim 580\text{--}620\text{ cm}^{-1}$  region. The normal modes associated with the  $\mu\text{OH}^-$  ligand as well couple to displacements in the Arg411 guanidinium group, due to the  $(\text{Arg411})\text{H}\cdots\text{O}(\text{H})$  hydrogen bonding (see animations separately available in the ESI).

The  $^{57}\text{Fe}$ -PVDOS fingerprints of the coordinating bridging hydroxyl ligand arise from the Ni/Fe– $\mu\text{OH}$  normal modes outlined above. These spectral features are discussed below in context of the  $\text{HoxC}_{\text{ai}}$  sample and the corresponding DFT model  $\text{Ni}_r\text{-S}_{\mu\text{OH}}^{\text{SH}}$  with  $\text{Ni}^{\text{II}}$  (while in the oxidized  $\text{Ni}^{\text{III}}$  state, the same character features commonly appear red-shifted). The Ni– $\mu\text{OH}$  stretching mode is associated with the NRVS-observed and DFT-calculated bands at  $507$  and  $506\text{ cm}^{-1}$  respectively (**Fig. S16a,b**); it is coupled to the Fe–CO/CN modes and  $(\text{Cys479})\text{S}$ –H bends. The Ni– $\mu\text{OH}$  stretch was found markedly sensitive to protonation states of the Ni-

terminal cysteines; in the alternative  $\text{Ni}_r\text{-S}_{\mu\text{OH}}^{\text{S}^-}$  model with deprotonated Cys479, this mode gets upshifted to  $523\text{ cm}^{-1}$ , producing band perturbations around  $\sim 500 - 530\text{ cm}^{-1}$  (as seen in **Fig. 5a, 6 bottom, S16c**). In the  $\text{Ni}_r\text{-S}_{\mu\text{OH}}^{\text{Cys60-SH}}$  model with a protonated Cys60, two upshifted Ni- $\mu\text{OH}$  stretches appear at  $538$  and  $560\text{ cm}^{-1}$ , which results in a distinct splitting of the high-intensity Fe-CO band at  $\sim 550\text{ cm}^{-1}$  (**Fig. 5b**). This effect is explained by strengthening of the Ni- $\mu\text{OH}$  bond upon the Cys60 protonation, enhanced by the *trans* (Cys60)S(H)-Ni(II)- $\mu\text{OH}^-$  coordination.

Unexpectedly, the Fe- $\mu\text{OH}$  stretch produces only a small  $^{57}\text{Fe}$ -PVDOS intensity, associated with the NRV/S/DFT features at  $427/424\text{ cm}^{-1}$  at the lower end of the Fe-CO/CN spectral region (**Fig. S16a, b**). The small Fe- $\mu\text{OH}$  intensity can be explained by (i) a *trans* effect in the symmetric OC-Fe- $\mu\text{OH}$  vibration at  $424\text{ cm}^{-1}$  (**Fig. S19d and Fig. 7**), compensating the  $^{57}\text{Fe}$  nucleus motion, as well as (ii) a relatively weak Fe- $\mu\text{OH}^-$  bonding to the hexacoordinated low-spin  $\text{Fe}^{\text{II}}$  center with two other strong-field  $\text{CN}^-$  ligands. Considering the optimized shorter Ni- $\mu\text{O}(\text{H}) = 1.90\text{ \AA}$  and longer Fe- $\mu\text{O}(\text{H}) = 2.04\text{ \AA}$  distances in the  $\text{Ni}_r\text{-S}_{\mu\text{OH}}^{\text{SH}}$  model, the mode at  $424\text{ cm}^{-1}$  can be also interpreted as a Ni- $\mu\text{OH}$  bending vibration.

Yet even lower vibrational energies in the  $\sim 250 - 340\text{ cm}^{-1}$  range and rather small  $^{57}\text{Fe}$ -PVDOS intensities were obtained for the Fe-( $\mu$ ) $\text{H}_2\text{O}$  stretching modes from the alternative models featuring either bridging ( $\text{Ni}_r\text{-S}_{\mu\text{H}_2\text{O}}^{\text{SH}}$  and  $\text{Ni}_r\text{-S}_{\mu\text{H}_2\text{O}}^{\text{S}^-}$ ) or terminal ( $\text{Ni}_r\text{-S}_{\text{Fe-H}_2\text{O}}^{\text{SH}}$  and  $\text{Ni}_r\text{-S}_{\text{Fe-H}_2\text{O}}^{\text{S}^-}$ ) water coordination. In spite of the absence of prominent stand-alone Fe- $\mu\text{OH}$  features, all three types of the Ni/Fe- $\text{H}_2\text{O}$  coordination presently tested (**Fig. S8-S10**) introduced significant perturbations in the high-intensity Fe-CO/CN region ( $\sim 400 - 620\text{ cm}^{-1}$ ), leading to vibrational patterns inconsistent with the NRV spectrum of HoxC<sub>ai</sub> (**Fig. 5**). This effect bears parallels to perturbations of the Fe-CO/CN region by deuteride (Fe-D) modes, which are similarly low in their inherent  $^{57}\text{Fe}$ -PVDOS intensity. Upon Fe-H to Fe-D labeling, these isotope-dependent NRV spectra perturbations have been earlier obtained for the Ni<sub>a</sub>-SR state of [NiFe]-hydrogenase,<sup>19</sup> for the H<sub>hyd</sub> state of [FeFe]-hydrogenase,<sup>20</sup> and for iron-hydride model complexes.<sup>21-23</sup>

Finally, the minimal model calculations (see DFT Methods) explored importance of explicit 2<sup>nd</sup>-shell interactions between the [NiFe]-cofactor and its protein environment, omitting all the residues except the four cysteines directly coordinating the two metal centers. The minimal model shared the same total charge, as well as the DFT methodology details, with the extended homology model. The minimal scheme was applied selectively to the states relevant to the NRV samples, yielding systems  $\text{Ni}_r\text{-S}_{\mu\text{OH}}^{\text{SH}}_{\text{MIN}}$  and  $\text{Ni}_r\text{-B}_{\mu\text{OH}}^{\text{SH}}_{\text{MIN}}$  (**Fig. S5**). Producing a displacement of the [NiFe] core relatively to the protein framework more prominent around

the Fe site, the minimal models deficit in a higher-quality reproduction of the experimental NRV spectra (**Fig. S18c**). Particularly the Fe–CO/CN region  $> 400\text{ cm}^{-1}$  becomes adversely affected, showing too large redox-dependent shifts of  $\sim 70\text{ cm}^{-1}$ .

### Supplementary Figures

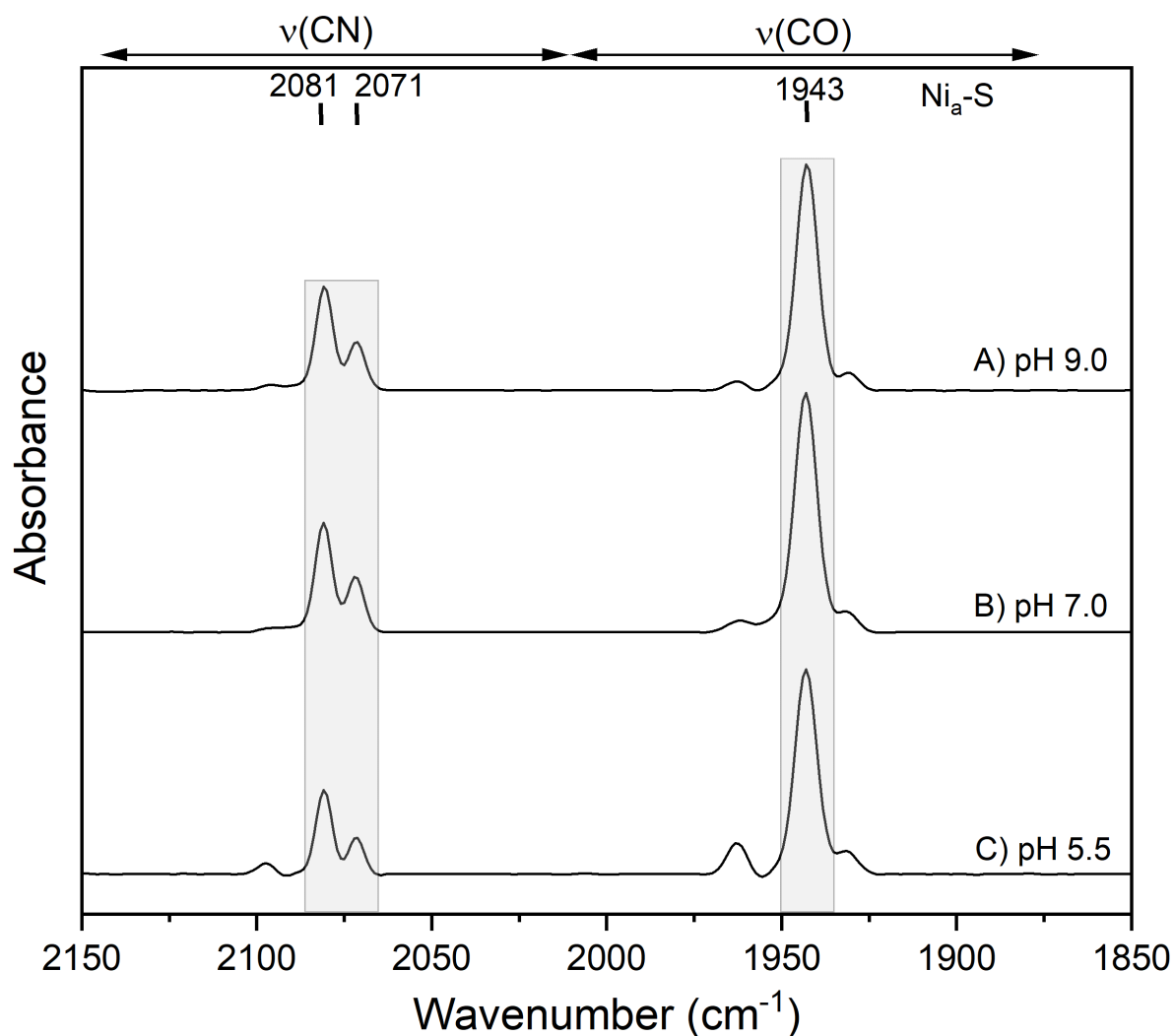


**Fig. S1** IR spectra of as-isolated RH recorded at 283 K and at different pH values showing the absorptions related to  $\nu(\text{CO})$  and  $\nu(\text{CN})$  stretching modes of the active site. The spectra are normalized to the protein concentration. RH samples named A, B and C were equilibrated at the desired pH value using a buffered solution consisting of 100 mM  $\text{K}_2\text{HPO}_4$  and 50 mM citric acid in addition to 150 mM NaCl.  $\nu(\text{CO})$ - and  $\nu(\text{CN})$ -related bands of the  $\text{Ni}_a\text{-S}$  state are marked by a grey rectangle.<sup>2</sup>

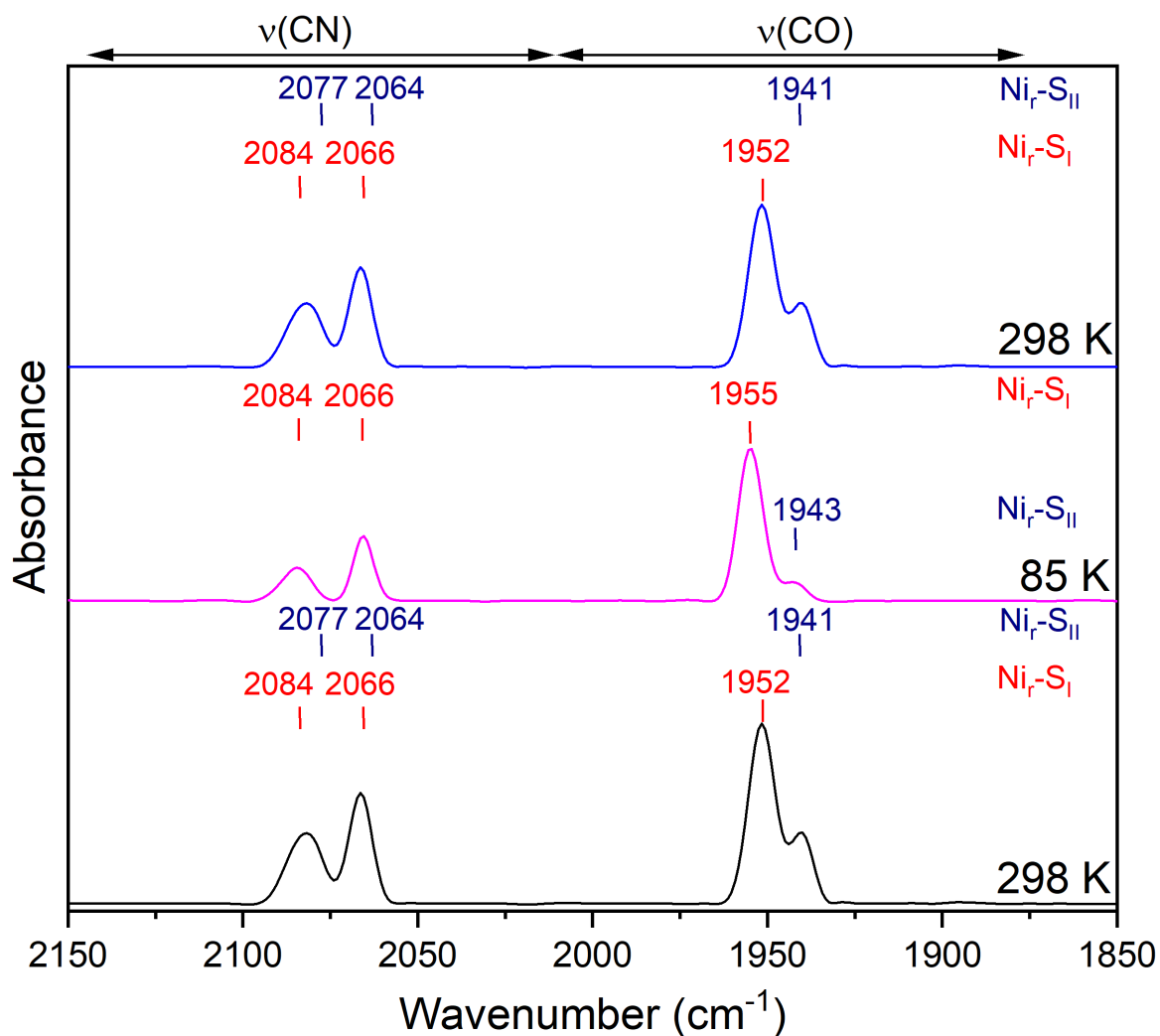


**Fig. S2** IR spectra of as-isolated HoxC (HoxC<sub>ait</sub>) recorded at different temperatures. A first spectrum was taken at 298 K (black trace), then the sample temperature was poised to 85 K (magenta trace) and, subsequently, the sample temperature was set back to 298 K (blue trace). Bands related to the ν(CO) and ν(CN) stretching modes of the diatomic ligands of the active site are labelled in red and dark blue, representing the Ni<sub>r</sub>-S<sub>I</sub> and Ni<sub>r</sub>-S<sub>II</sub> species, respectively. Lowering the temperature resulted in an enrichment of the Ni<sub>r</sub>-S<sub>I</sub> species population. This process is reversible, as the initial Ni<sub>r</sub>-S<sub>I</sub> and Ni<sub>r</sub>-S<sub>II</sub> ratio was restored by heating up the sample to room temperature.

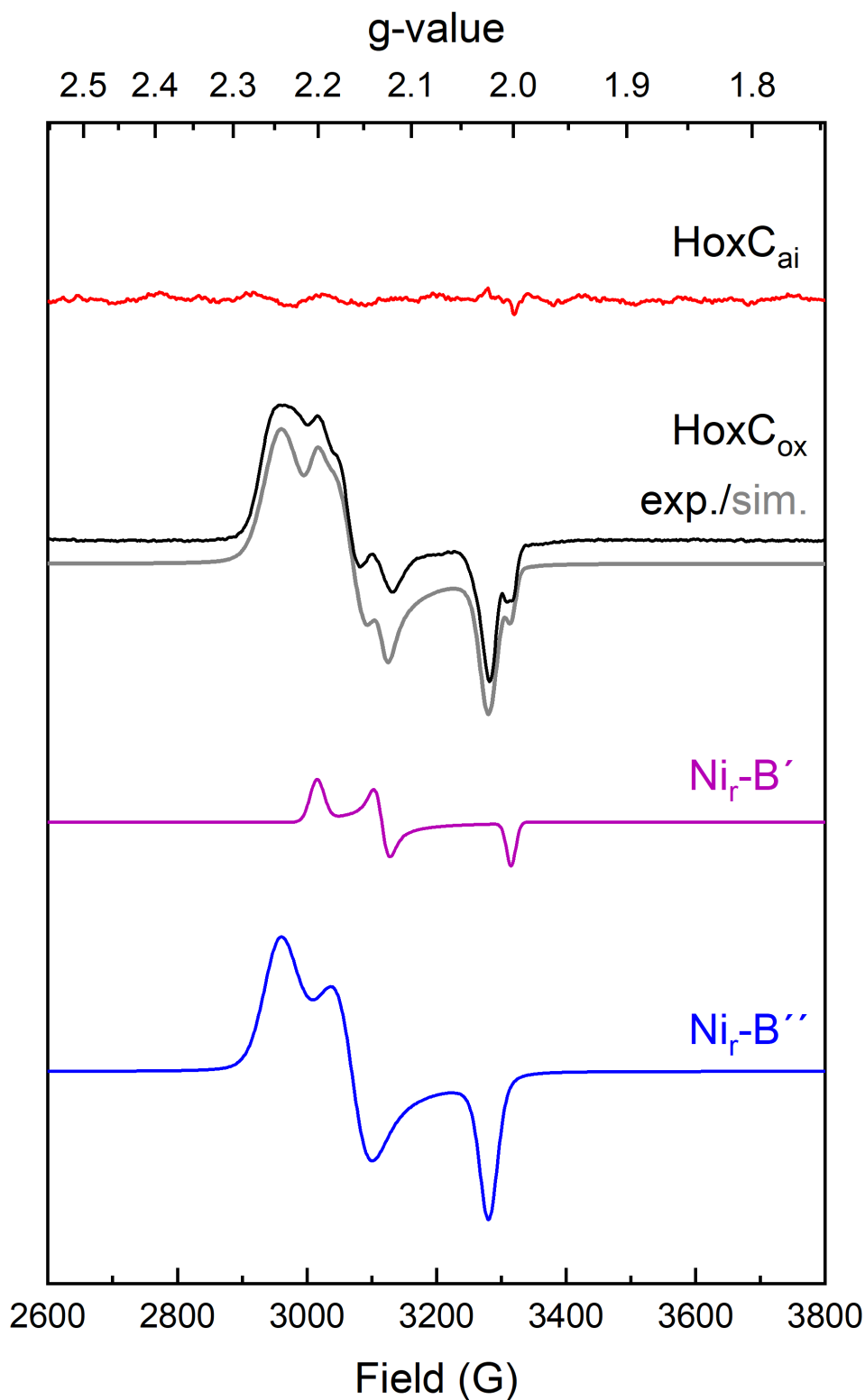


**Fig. S3** EPR spectra of HoxC<sub>ai</sub> and chemically oxidized HoxC<sub>ox</sub> measured at 20 K. Depicted is the EPR spectrum of diamagnetic, HoxC<sub>ai</sub> (red trace) and that of paramagnetic HoxC<sub>ox</sub> together with the corresponding simulations (black and grey traces). The spectrum of HoxC<sub>ox</sub> was simulated assuming a minor species denoted Ni<sub>r</sub>-B' (violet trace, g values:  $g_x = 2.203$ ,  $g_y = 2.132$ ,  $g_z = 2.004$ ) and a major Ni<sub>r</sub>-B'' species (blue trace, g values:  $g_x = 2.246$ ,  $g_y = 2.164$ ,  $g_z = 2.025$ ). HoxC<sub>ox</sub> was prepared by adding three equivalents of K<sub>3</sub>Fe(CN)<sub>6</sub> to HoxC<sub>ai</sub>.<sup>2</sup>

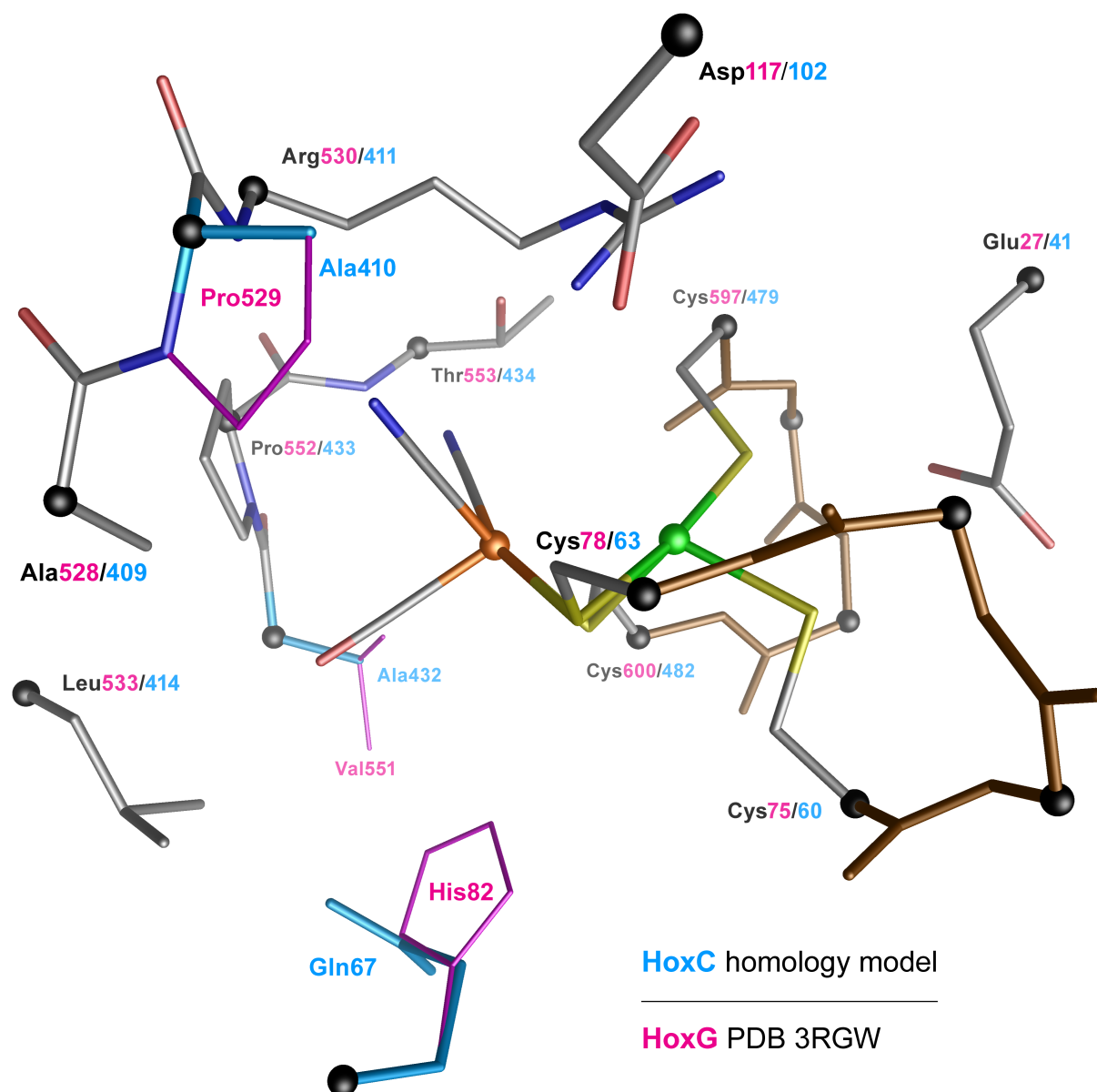


**Fig. S4** Homology model of the HoxC active site and its adjacent protein environment, which was used for the DFT calculations. The model is based on the X-ray structure of the large subunit HoxG from the membrane-bound [NiFe]-hydrogenase (MBH) of *R. eutropha* (PDB 3RGW).<sup>9</sup> Model-related amino acid conflicts in HoxG vs HoxC are (shown correspondingly in magenta vs blue): His82 vs Gln67, Pro529 vs Ala410, and Val551 vs Ala432. Two conserved HoxG/HoxC backbone fragments were included in the model (shown in brown), each of them embraced two amino acids by two Cys residues coordinating the Ni center: Cys75/60-X-X-Cys78/63 and Cys597/479-X-X-Cys600/482. The amino acids included in the model are labeled according to the HoxG (magenta) and HoxC (blue) numbering. The C<sub>α</sub> carbon nuclei and the two metals are shown in ball representation.

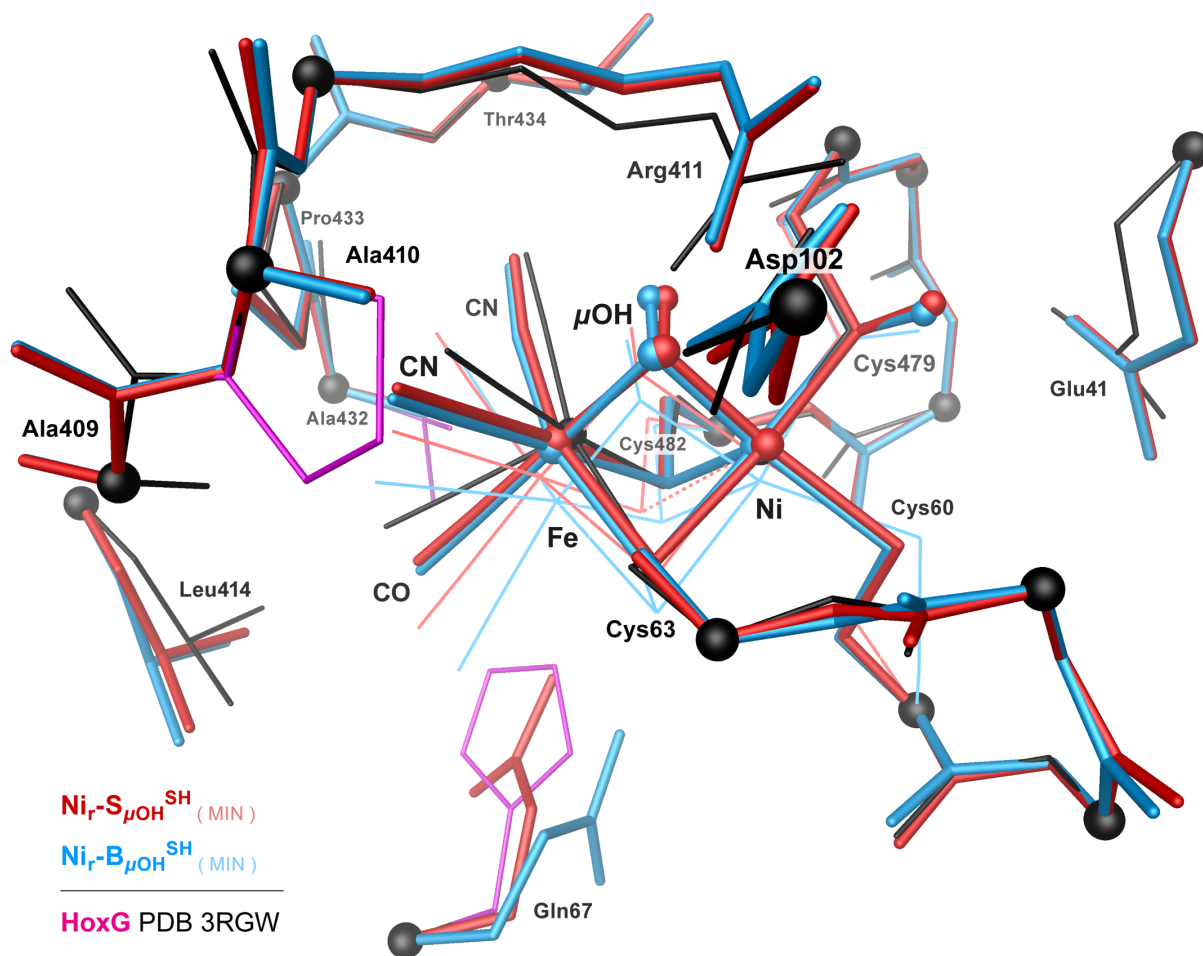


**Fig. S5** Best-fitting DFT-optimized HoxC models for the Ni<sub>r</sub>-S<sub>I</sub> (model Ni<sub>r</sub>-S<sub>μOH</sub><sup>SH</sup>, red, thick tubes) and Ni<sub>r</sub>-B'' (model Ni<sub>r</sub>-B<sub>μOH</sub><sup>SH</sup>, blue, thick tubes) states, both containing a bridging μOH<sup>-</sup> ligand and a protonated Ni-bound Cys479 cysteine. Additionally, minimal models Ni<sub>r</sub>-S<sub>μOH</sub><sup>SH</sup><sub>MIN</sub> and Ni<sub>r</sub>-B<sub>μOH</sub><sup>SH</sup><sub>MIN</sub> are shown in corresponding colors and wire representations. The models were superimposed with the reference X-ray structure (black, thin tubes), i.e. the large subunit (HoxG) of the membrane-bound [NiFe]-hydrogenase (MBH) from *R. eutropha* (PDB 3RGW).<sup>9</sup> The HoxG amino acids which make conflicts with the HoxC sequence are colored in magenta. The shown amino acid labels and numbers are for the HoxC sequence. C<sub>α</sub> carbon nuclei, which were fixed during structure optimization to their reference positions in the X-ray structure, the two metal ions, the μOH<sup>-</sup> ligand, and the Cys479 protonation are shown in ball representation. The other protons are not displayed for clarity.

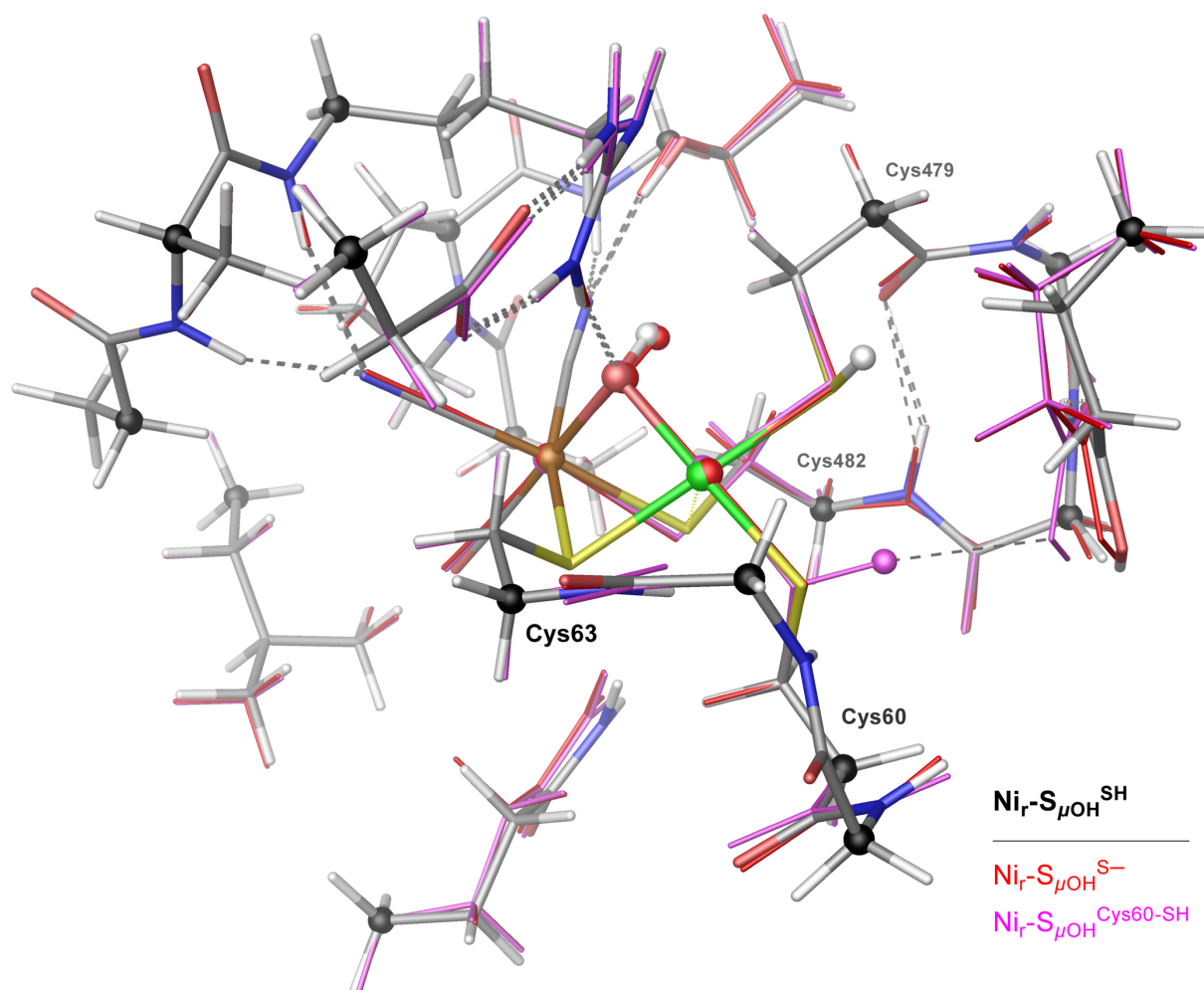


**Fig. S6** DFT-optimized models of the Ni<sub>r</sub>-S resting state containing a bridging  $\mu\text{OH}^-$  ligand and either protonated (best-fit model Ni<sub>r</sub>-S <sub>$\mu\text{OH}^{\text{SH}}$</sub> , element colors, thick tubes) or deprotonated (alternative model Ni<sub>r</sub>-S <sub>$\mu\text{OH}^{\text{S}^-}$</sub> , red, thin tubes) Cys479. A second alternative model contained Cys60 in its protonated form (alternative model Ni<sub>r</sub>-S <sub>$\mu\text{OH}^{\text{Cys60-SH}}$</sub> , magenta, thin tubes). C <sub>$\alpha$</sub>  carbon nuclei, which remained fixed during structure optimization, the two metal centers, the  $\mu\text{OH}^-$  ligand, and the Cys479/Cys60 protonation (respectively in Ni<sub>r</sub>-S <sub>$\mu\text{OH}^{\text{SH}}$</sub>  / Ni<sub>r</sub>-S <sub>$\mu\text{OH}^{\text{Cys60-SH}}$</sub> ) are shown in ball representation. The four active site cysteine residues are numbered according to the HoxC amino acid sequence. Element colors: C (gray), H (white), N (blue), O (red), Fe (brown), S (yellow), Ni (green).

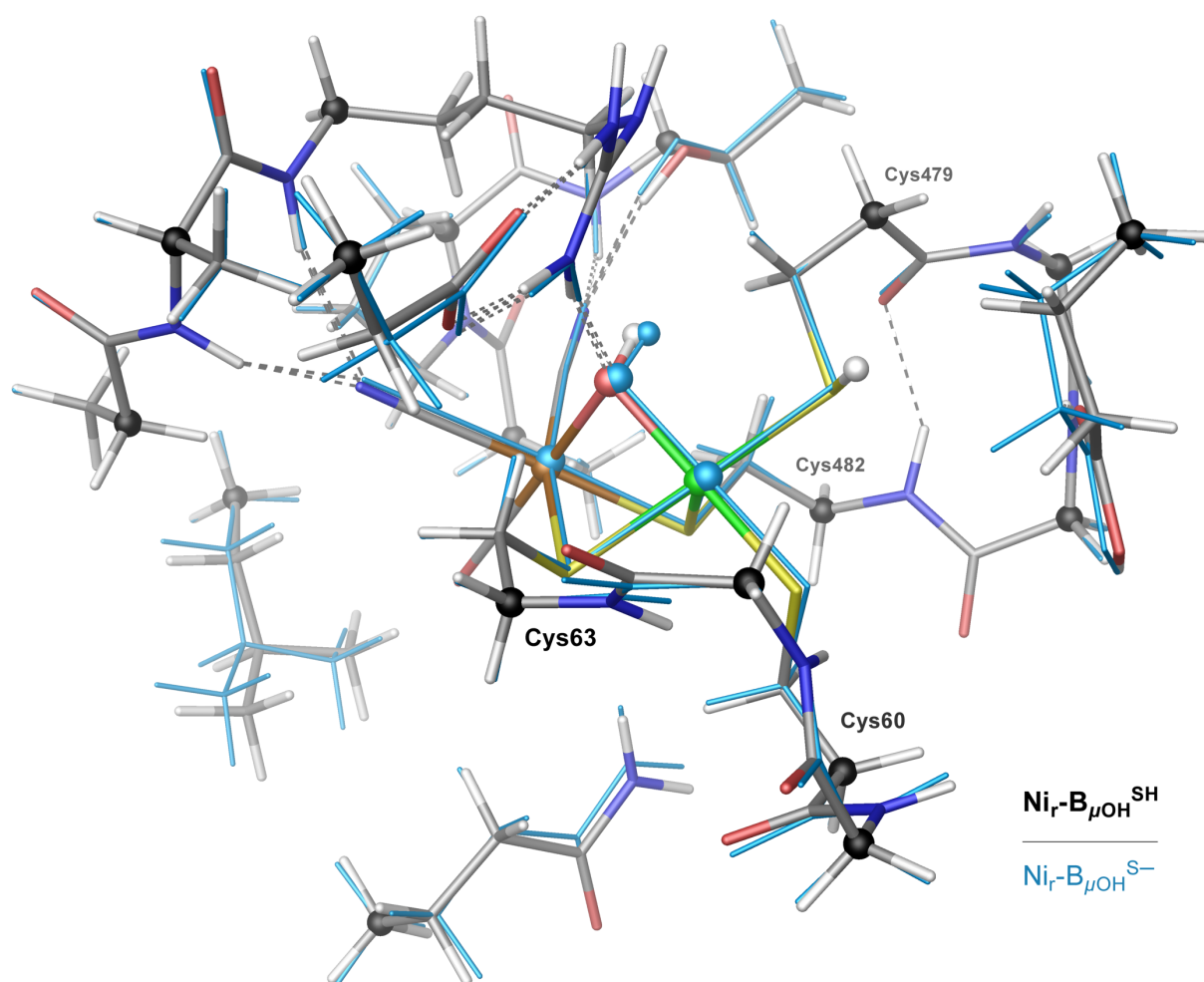


**Fig. S7** DFT-optimized models of the Ni<sub>r</sub>-B resting state containing a bridging  $\mu\text{OH}^-$  ligand and either protonated (best-fitting model Ni<sub>r</sub>-B $_{\mu\text{OH}}^{\text{SH}}$ , element colors, thick tubes) or deprotonated (alternative model Ni<sub>r</sub>-B $_{\mu\text{OH}}^{\text{S}^-}$ , blue, thin tubes) Cys479. C<sub>α</sub> carbon nuclei, which remained fixed during structure optimization, the two metal centers, the  $\mu\text{OH}^-$  ligand, and the Cys479 protonation (in Ni<sub>r</sub>-B $_{\mu\text{OH}}^{\text{SH}}$ ) are shown in ball representation. The four active site cysteine residues are numbered according to the HoxC amino acid sequence. Element colors: C (gray), H (white), N (blue), O (red), Fe (brown), S (yellow), Ni (green).

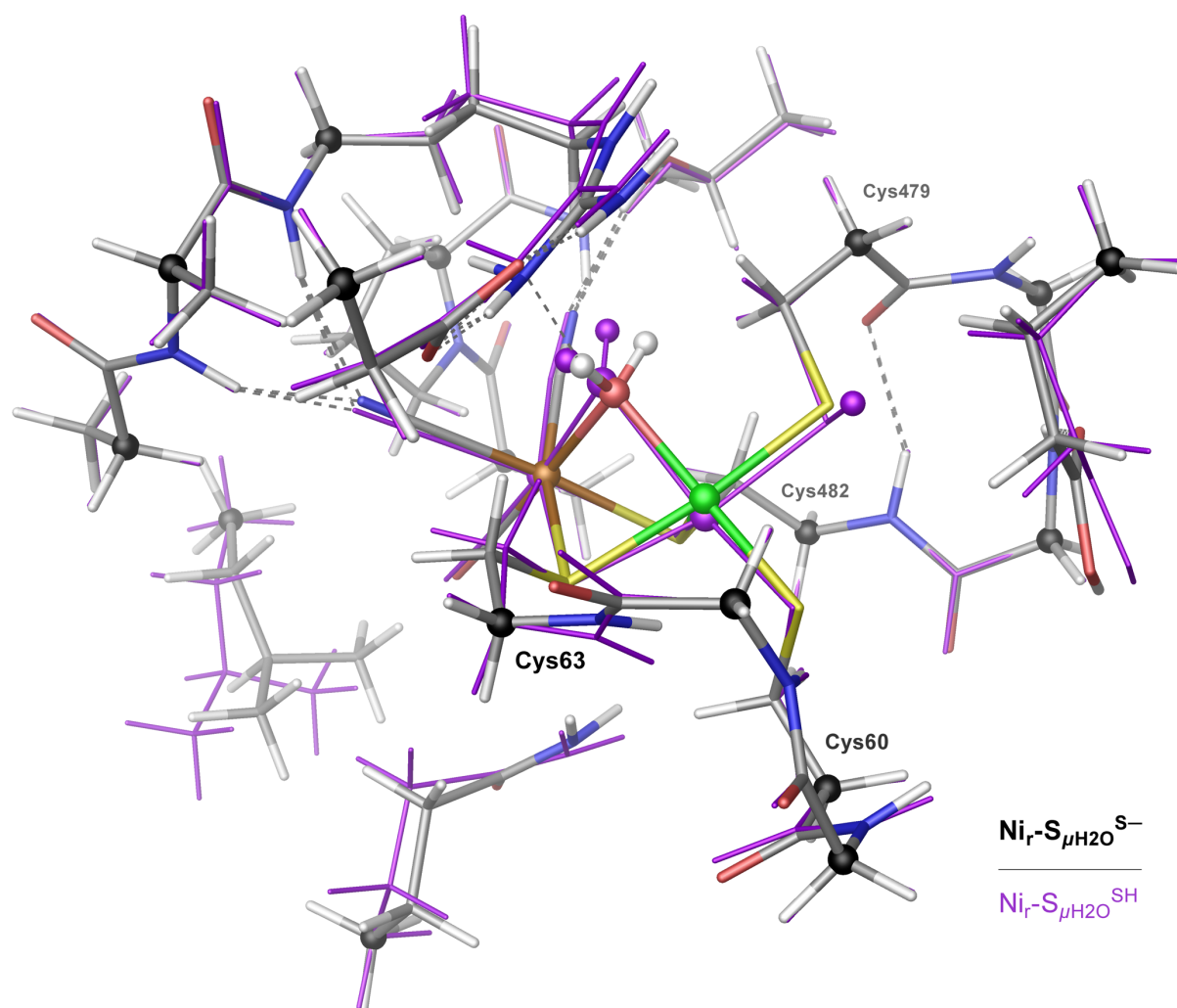


**Fig. S8** Alternative DFT-optimized models of the  $\text{Ni}_r\text{-S}$  state containing a bridging  $\mu\text{H}_2\text{O}$  ligand and either deprotonated (model  $\text{Ni}_r\text{-S}_{\mu\text{H}_2\text{O}}^{\text{S}^-}$ , element colors, thick tubes) or protonated (model  $\text{Ni}_r\text{-S}_{\mu\text{H}_2\text{O}}^{\text{SH}}$ , violet, thin tubes) Cys479.  $\text{C}_\alpha$  carbon nuclei, which remained fixed during structure optimization, the two metal centers, the  $\mu\text{H}_2\text{O}$  ligand, and the Cys479 protonation (in  $\text{Ni}_r\text{-S}_{\mu\text{H}_2\text{O}}^{\text{SH}}$ ) are shown in ball representation. The four active site cysteine residues are numbered according to the HoxC amino acid sequence. Element colors: C (gray), H (white), N (blue), O (red), Fe (brown), S (yellow), Ni (green).

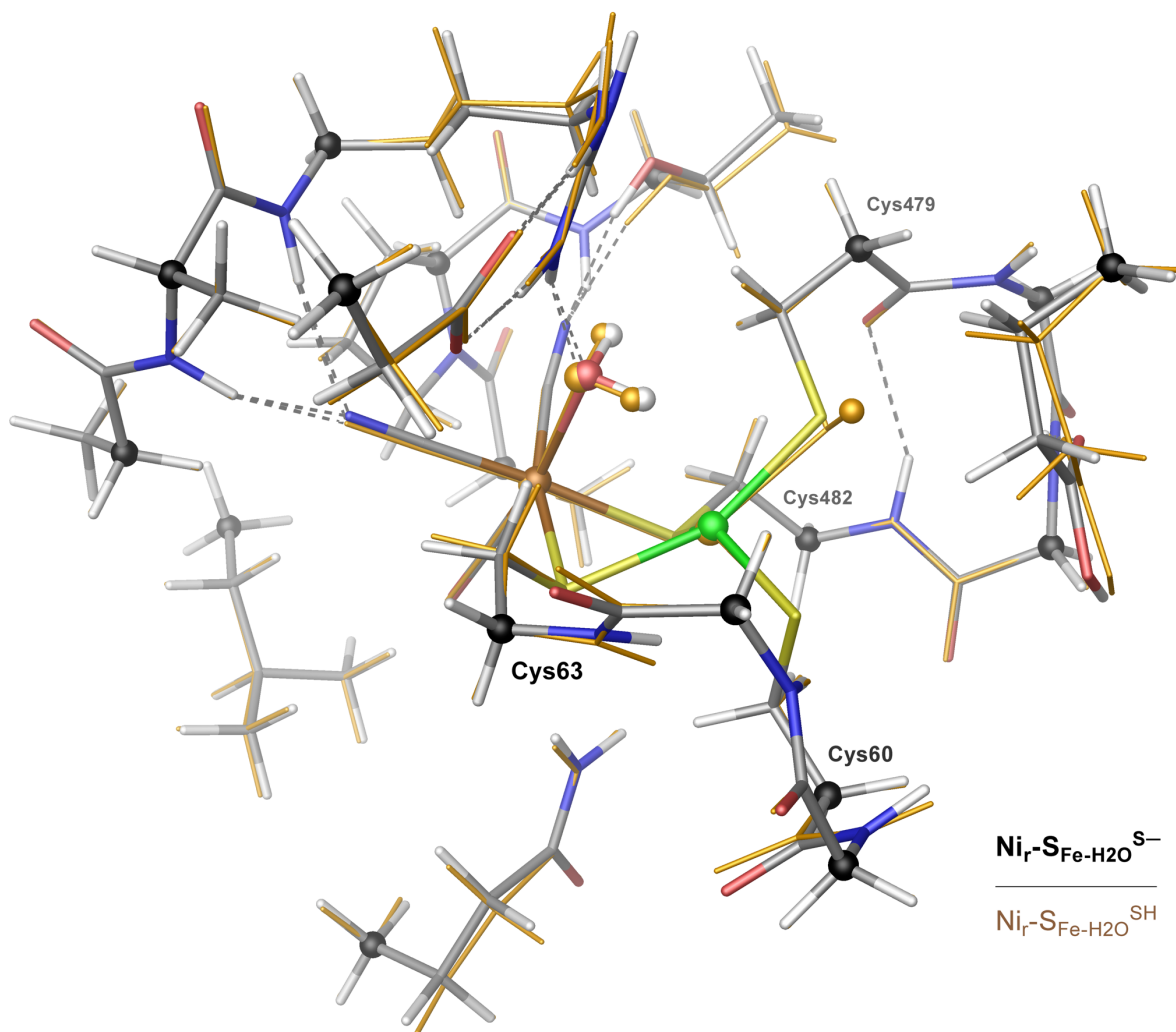


**Fig. S9** Alternative DFT-optimized models of the  $\text{Ni}_r\text{-S}$  state containing an Fe-bound terminal  $\text{H}_2\text{O}$  ligand and either deprotonated (model  $\text{Ni}_r\text{-S}_{\text{Fe-H}_2\text{O}}^{\text{S}^-}$ , element colors, thick tubes) or protonated (model  $\text{Ni}_r\text{-S}_{\text{Fe-H}_2\text{O}}^{\text{SH}}$ , beige, thin tubes) Cys479.  $\text{C}_\alpha$  carbon nuclei, which remained fixed during structure optimization, the two metal centers, the  $\text{H}_2\text{O}$  ligand, and the Cys479 protonation (in  $\text{Ni}_r\text{-S}_{\text{Fe-H}_2\text{O}}^{\text{SH}}$ ) are shown in ball representation. The four active site cysteine residues are numbered according to the HoxC amino acid sequence. Element colors: C (gray), H (white), N (blue), O (red), Fe (brown), S (yellow), Ni (green).

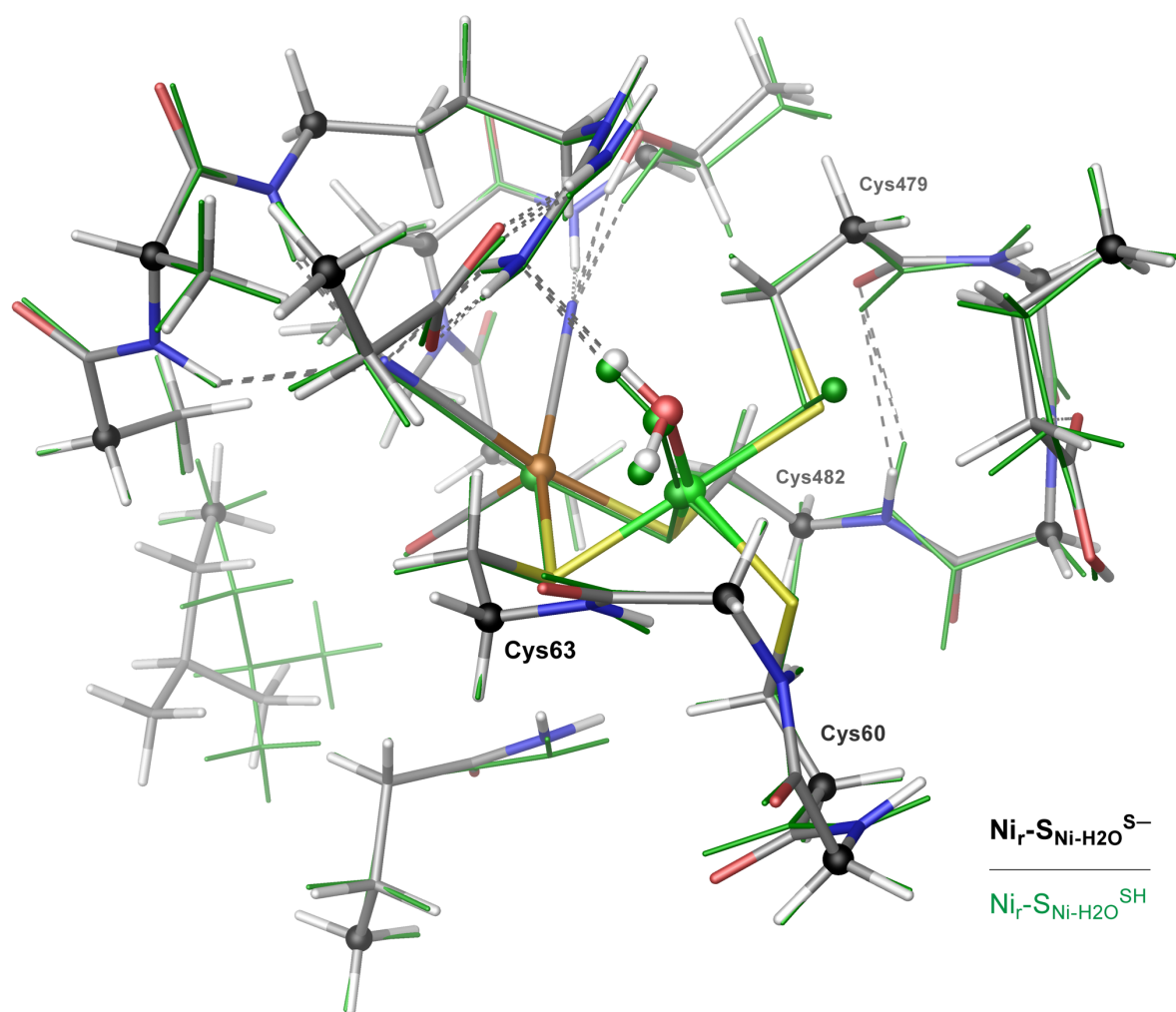


**Fig. S10** Alternative DFT-optimized models of the  $\text{Ni}_r\text{-S}$  state containing a terminal  $\text{H}_2\text{O}$  ligand and either deprotonated (model  $\text{Ni}_r\text{-S}_{\text{Ni-H}_2\text{O}}^{\text{S}^-}$ , element colors, thick tubes) or protonated (model  $\text{Ni}_r\text{-S}_{\text{Ni-H}_2\text{O}}^{\text{SH}}$ , green, thin tubes) Cys479.  $\text{C}_\alpha$  carbon nuclei, which remained fixed during structure optimization, the two metal centers, the  $\text{H}_2\text{O}$  ligand, and the Cys479 protonation (in  $\text{Ni}_r\text{-S}_{\text{Ni-H}_2\text{O}}^{\text{SH}}$ ) are shown in ball representation. The four active site cysteine residues are numbered according to the HoxC amino acid sequence. Element colors: C (gray), H (white), N (blue), O (red), Fe (brown), S (yellow), Ni (green).

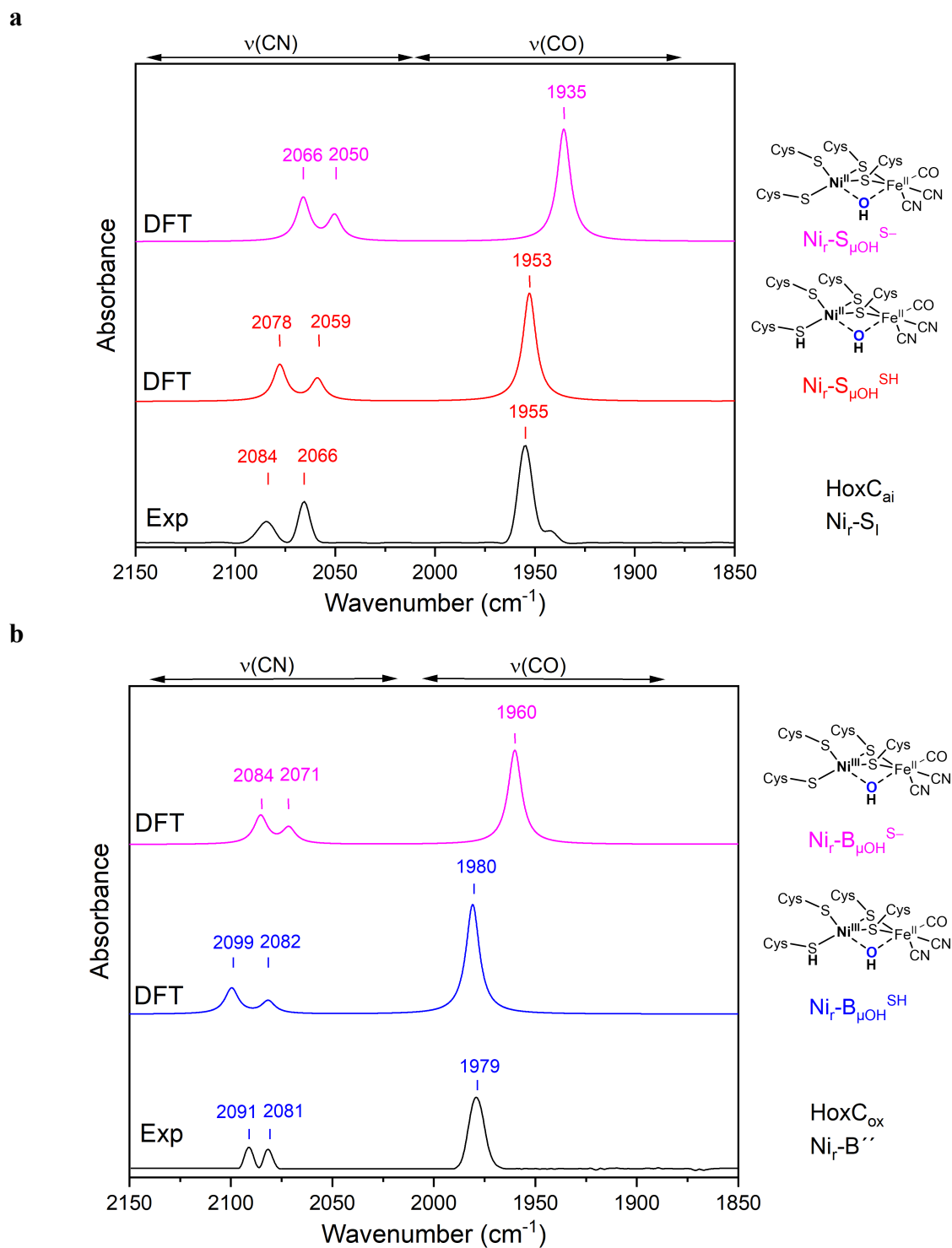


**Fig. S11** Experimental low-temperature and DFT-computed IR spectra displaying bands related to the CO and CN<sup>-</sup> ligands of the active site in the HoxC<sub>ai</sub> and HoxC<sub>ox</sub> proteins. **a.** Ni<sub>r</sub>-S<sub>μOH</sub><sup>SH</sup> (red trace) and Ni<sub>r</sub>-S<sub>μOH</sub><sup>S<sup>-</sup></sup> (magenta trace) models, harboring either protonated or deprotonated C479 and a bridging μOH<sup>-</sup> ligand, were used to compute the Ni<sub>r</sub>-S<sub>i</sub> species in HoxC<sub>ai</sub>. **b.** Ni<sub>r</sub>-B<sub>μOH</sub><sup>SH</sup> (blue trace) and Ni<sub>r</sub>-B<sub>μOH</sub><sup>S<sup>-</sup></sup> (magenta trace) models, containing either protonated or deprotonated C479 and a bridging μOH<sup>-</sup> ligand, were used to compute the Ni<sub>r</sub>-B<sup>''</sup> species in HoxC<sub>ox</sub>.

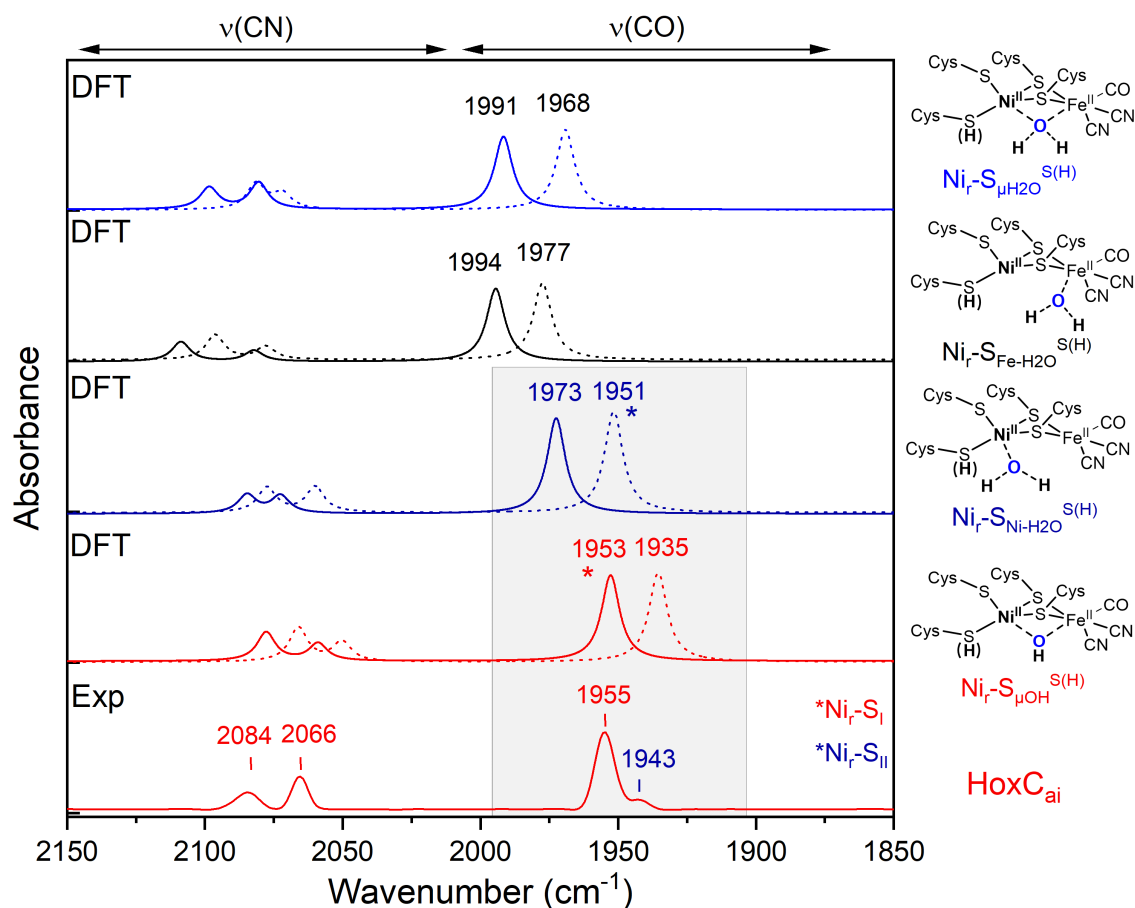


**Fig. S12** Low-temperature IR spectra of HoxC<sub>ai</sub> residing in the Ni<sub>r</sub>-S<sub>I</sub> and Ni<sub>r</sub>-S<sub>II</sub> resting states in comparison to DFT-predicted infrared bands using different Ni<sub>r</sub>-S models of the active site. The DFT-computed spectra were generated using models comprising either protonated (solid lines) or deprotonated C479 (dotted line). Color code: red, Ni<sub>r</sub>-S<sub>μOH</sub><sup>SH</sup> and Ni<sub>r</sub>-S<sub>μOH</sub><sup>S-</sup> (models are depicted in **Fig. S6**); dark blue, Ni<sub>r</sub>-S<sub>Ni-H2O</sub><sup>SH</sup> and Ni<sub>r</sub>-S<sub>Ni-H2O</sub><sup>S-</sup> (models are depicted in **Fig. S10**); black, Ni<sub>r</sub>-S<sub>Fe-H2O</sub><sup>SH</sup> and Ni<sub>r</sub>-S<sub>Fe-H2O</sub><sup>S-</sup> (models are depicted in **Fig. S9**); blue, Ni<sub>r</sub>-S<sub>μH2O</sub><sup>SH</sup> and Ni<sub>r</sub>-S<sub>μH2O</sub><sup>S-</sup> (models are depicted in **Fig. S8**). For models Ni<sub>r</sub>-S<sub>μH2O</sub><sup>SH</sup>/Ni<sub>r</sub>-S<sub>μH2O</sub><sup>S-</sup>/Ni<sub>r</sub>-S<sub>Fe-H2O</sub><sup>SH</sup>, the DFT calculations revealed additional Arg411-Asp102 bands in the 2070-2150 cm<sup>-1</sup> region that have been considered as an artifact and were subtracted from the shown spectra. The computed IR spectrum based on the Ni<sub>r</sub>-S<sub>μOH</sub><sup>Cys60-SH</sup> model (**Fig. S6**) is almost identical to the computed IR spectrum based on the Ni<sub>r</sub>-S<sub>μOH</sub><sup>SH</sup> model and is not shown for the sake of clarity. The experimental CO absorptions of HoxC<sub>ai</sub>, i.e. 1955 cm<sup>-1</sup> for Ni<sub>r</sub>-S<sub>I</sub> and at 1943 cm<sup>-1</sup> for Ni<sub>r</sub>-S<sub>II</sub>, are best reproduced by the models Ni<sub>r</sub>-S<sub>μOH</sub><sup>SH</sup> (1953 cm<sup>-1</sup>) and Ni<sub>r</sub>-S<sub>Ni-H2O</sub><sup>S-</sup> (1951 cm<sup>-1</sup>) (highlighted by asterisks). None of the other models reproduced the experimentally observed red-shift for the Ni<sub>r</sub>-S<sub>II</sub> species with respect to Ni<sub>r</sub>-S<sub>I</sub>. The experimental 12 cm<sup>-1</sup> shift is too small to account for a charge change at the active site. Thus, the data suggest that the Ni<sub>r</sub>-S<sub>I</sub> and Ni<sub>r</sub>-S<sub>II</sub> species represent isomers with the same charge but an alternative proton localization. Previous IR results obtained at low pH and room temperature can be interpreted with a proton migration from the (protonated) cysteine C479 of HoxC<sub>ai</sub> to the bridging hydroxyl ligand, resulting in the formation of a terminal water ligand bound to the Ni ion (**Fig. 1**).<sup>2</sup>

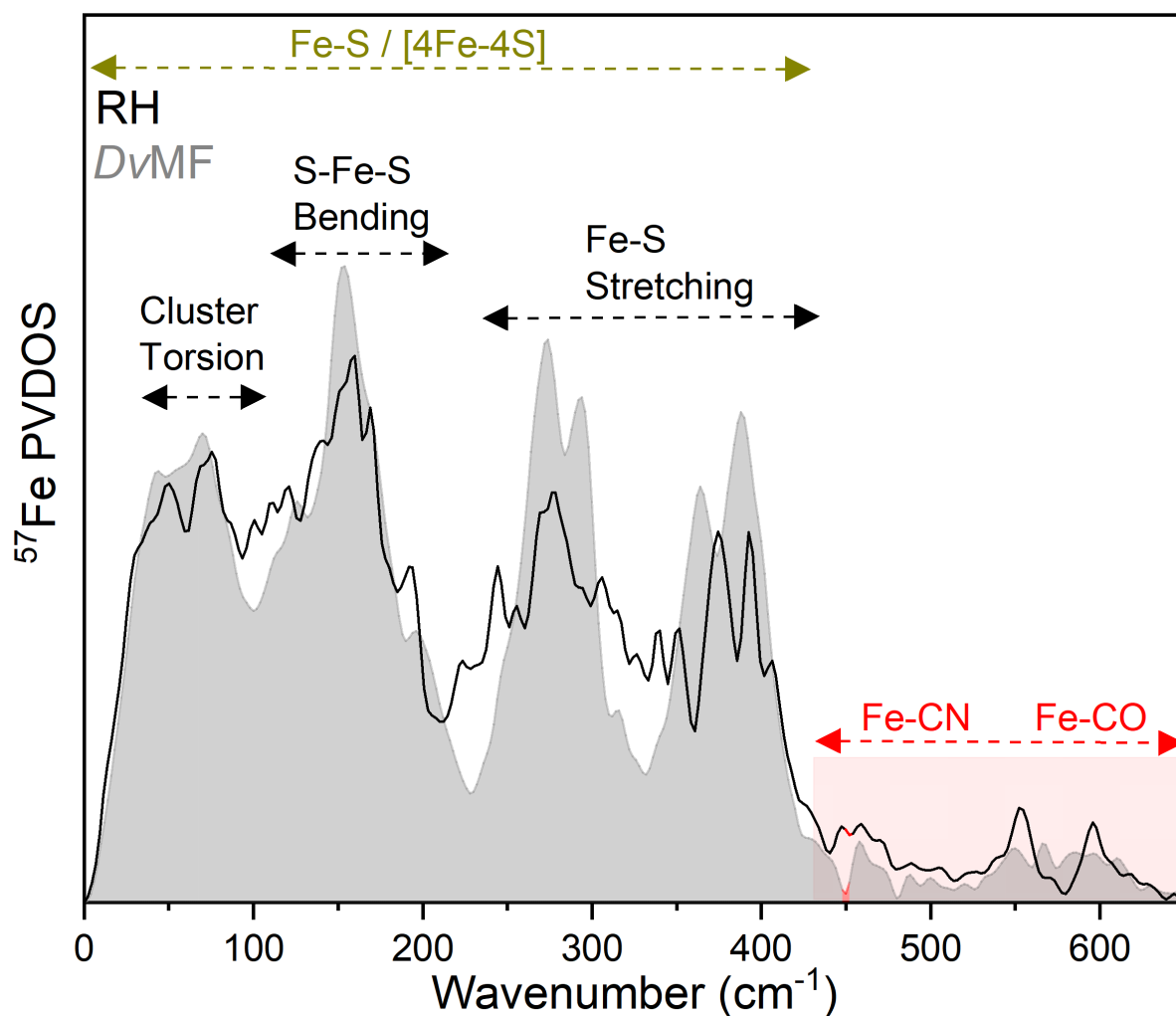


**Fig. S13** NRVS data recorded on the [ $^{57}\text{Fe}$ ]-enriched *DvMF* [NiFe]-hydrogenase in the  $\text{Ni}_u\text{-A}$  state (grey) and [ $^{57}\text{Fe}$ ]-enriched RH in the  $\text{Ni}_a\text{-S}$  state (black trace). The spectra display major contributions from the FeS clusters ( $0 - 420 \text{ cm}^{-1}$ , marked with an olive arrow), including [4Fe4S] cluster-derived torsional modes, S-Fe-S bending, and Fe-S stretching vibrations.<sup>18</sup> Spectral contributions from the active site are exclusively visible in the high-frequency region ranging from  $420 \text{ cm}^{-1}$  to  $600 \text{ cm}^{-1}$  (light red rectangle).

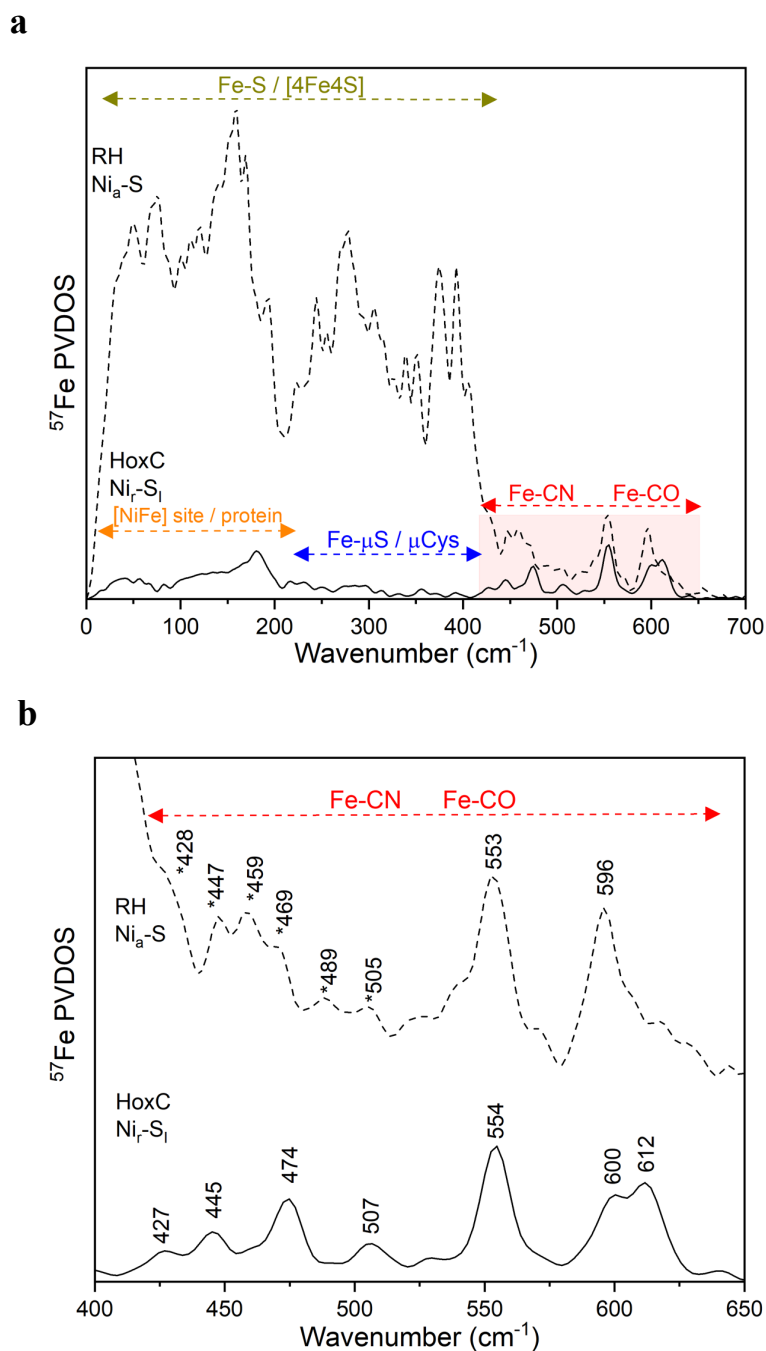


**Fig. S14** NRV spectra of  $^{57}\text{Fe}$ -enriched RH and HoxC. **a.** NRVS data of  $^{57}\text{Fe}$ -enriched RH in the  $\text{Ni}_a\text{-S}$  state (dashed line) and of  $^{57}\text{Fe}$ -enriched HoxC<sub>ai</sub> in the  $\text{Ni}_r\text{-S}_I$  state (full line). Both spectra are normalized with respect to the iron content. **b.** Blow up of the 400-650  $\text{cm}^{-1}$  region of **Fig. S14a**. The spectral regions containing bands derived from Fe–CO and Fe–CN modes of the active site, from Fe–S modes of the [4Fe4S] clusters, from the active site / protein modes, and from Fe- $\mu\text{S}$  modes involving bridging cysteines are marked with red, olive, orange, and blue arrows, respectively. Dominant bands in panel B are labelled with the corresponding peak positions. Bands marked with an asterisk could not be properly resolved, due to their low absolute intensity (see **Fig. 4** for a comparison of the active site bands of RH and HoxC<sub>ai</sub>) or due to overlapping bands. Error bars have been omitted for clarity. The corresponding NRVS data including error bars are displayed in **Fig. S20**.

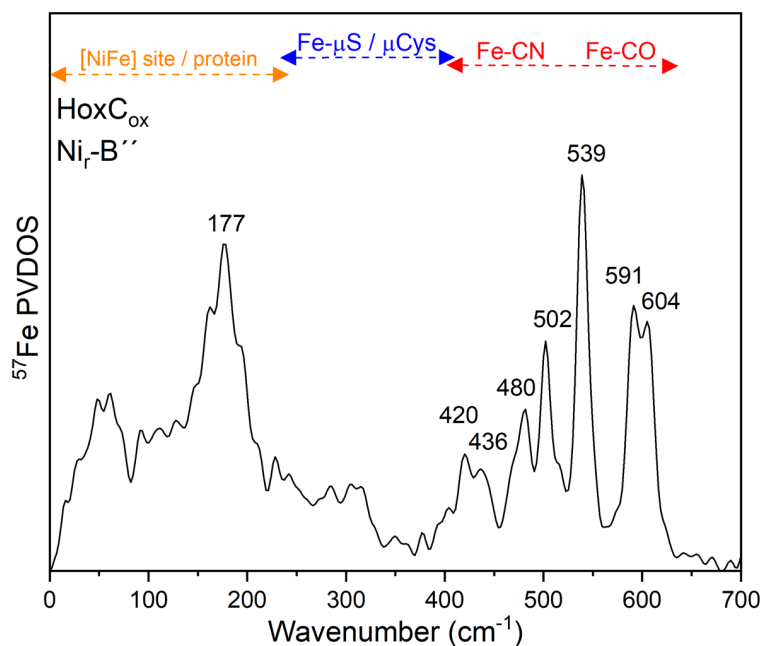


**Fig. S15** Experimental NRV spectrum of  $^{57}\text{Fe}$ -enriched  $\text{HoxC}_{\text{ox}}$  protein. The spectral regions containing bands related to mainly Fe-CO and Fe-CN modes of the active site, to active site/protein modes, and to Fe- $\mu\text{S}$  modes involving bridging cysteines are marked by red, orange and blue arrows respectively. Most relevant bands are labelled with the corresponding position of the peak maximum. Error bars have been omitted for clarity. The corresponding NRVS data including error bars are shown in **Fig. S20**. Ferricyanide,  $\text{Fe}(\text{CN})_6^{3-}$ , was used as oxidant and almost completely converted into reduced, diamagnetic ferrocyanide ( $\text{Fe}(\text{CN})_6^{4-}$ ). Hence, spectral contributions from the Fe-CN modes of ferrocyanide are to be expected. Previous data recorded on  $\text{Fe}(\text{CN})_6^{4-}$  revealed that the most intense Fe-CN band occurs at  $600\text{ cm}^{-1}$ .<sup>24</sup> However, considering that the natural abundance of  $^{57}\text{Fe}$  is only 2.2%, only  $60 - 70\ \mu\text{M}$   $^{57}\text{Fe}(\text{CN})_6^{4-}$  would be present in the oxidized sample ( $\text{HoxC}_{\text{ox}} \approx 1.2\ \text{mM}$ ). Therefore, bands of ferrocyanide are either under the detection limit or hidden by the prominent active site bands of  $\text{HoxC}_{\text{ox}}$ .

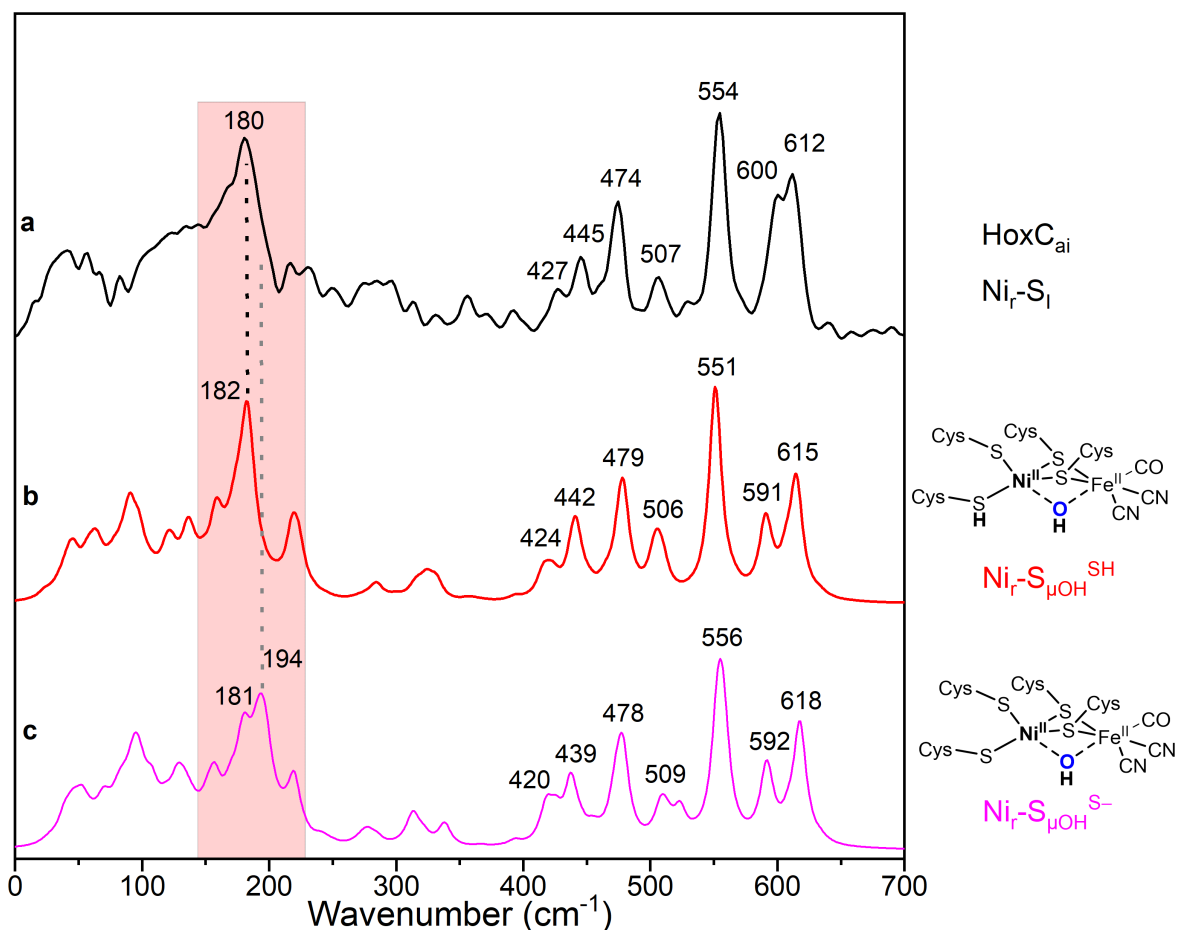


**Fig. S16** Comparison of the experimental NRV spectrum of HoxC<sub>ai</sub> with computed spectra derived from different active site models. The experimental NRV spectrum of a <sup>57</sup>Fe-enriched HoxC<sub>ai</sub> sample in the Ni<sub>r</sub>-S<sub>I</sub> state is shown in trace **a**. DFT-predicted <sup>57</sup>Fe-PVDOS spectra of the active site based on the Ni<sub>r</sub>-S<sub>μOH</sub><sup>SH</sup> and Ni<sub>r</sub>-S<sub>μOH</sub><sup>S<sup>-</sup></sup> models (**Fig. S6**), are shown in traces **b** and **c**, respectively. Minor differences in the low-frequency region (highlighted by dashed black and grey lines in the light red box), are supportive of the Ni<sub>r</sub>-S<sub>μOH</sub><sup>SH</sup> model. All other models, displayed in **Fig. S8-S10**, provided alternative <sup>57</sup>Fe-PVDOS signatures, exhibiting an inferior match to the observed HoxC<sub>ai</sub> spectrum (**Fig. 5**).

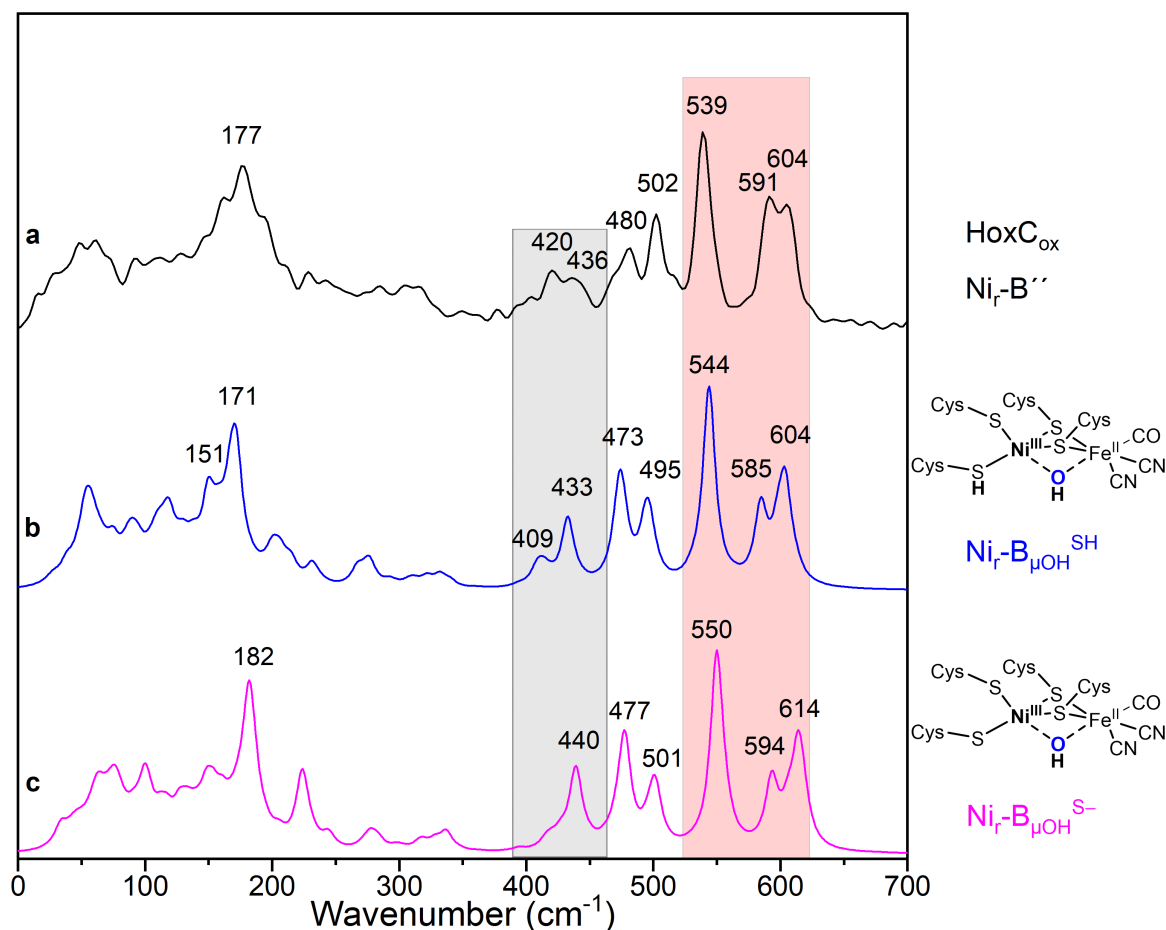


**Fig. S17** Comparison of the experimental NRV spectrum of HoxC<sub>ox</sub> with computed spectra derived from different active site models. The experimental NRV spectrum of a <sup>57</sup>Fe-enriched HoxC<sub>ox</sub> sample in the Ni<sub>r</sub>-B'' state is shown in trace a. DFT-predicted <sup>57</sup>Fe-PVDOS spectra of the active site based on the Ni<sub>r</sub>-B<sub>μOH</sub><sup>SH</sup> and Ni<sub>r</sub>-B<sub>μOH</sub><sup>S-</sup> models (Fig. S7), are shown in traces b and c, respectively. Bands residing in the 400 – 450 cm<sup>-1</sup> region (grey box) are better reproduced by the Ni<sub>r</sub>-B<sub>μOH</sub><sup>SH</sup> model, which also showed a closer match to the predominant Fe–CO bands in the 550 – 610 cm<sup>-1</sup> region (light red box). The data strengthen the Ni<sub>r</sub>-B<sub>μOH</sub><sup>SH</sup> model with a protonated cysteine Cys479 for the Ni<sub>r</sub>-B'' state.

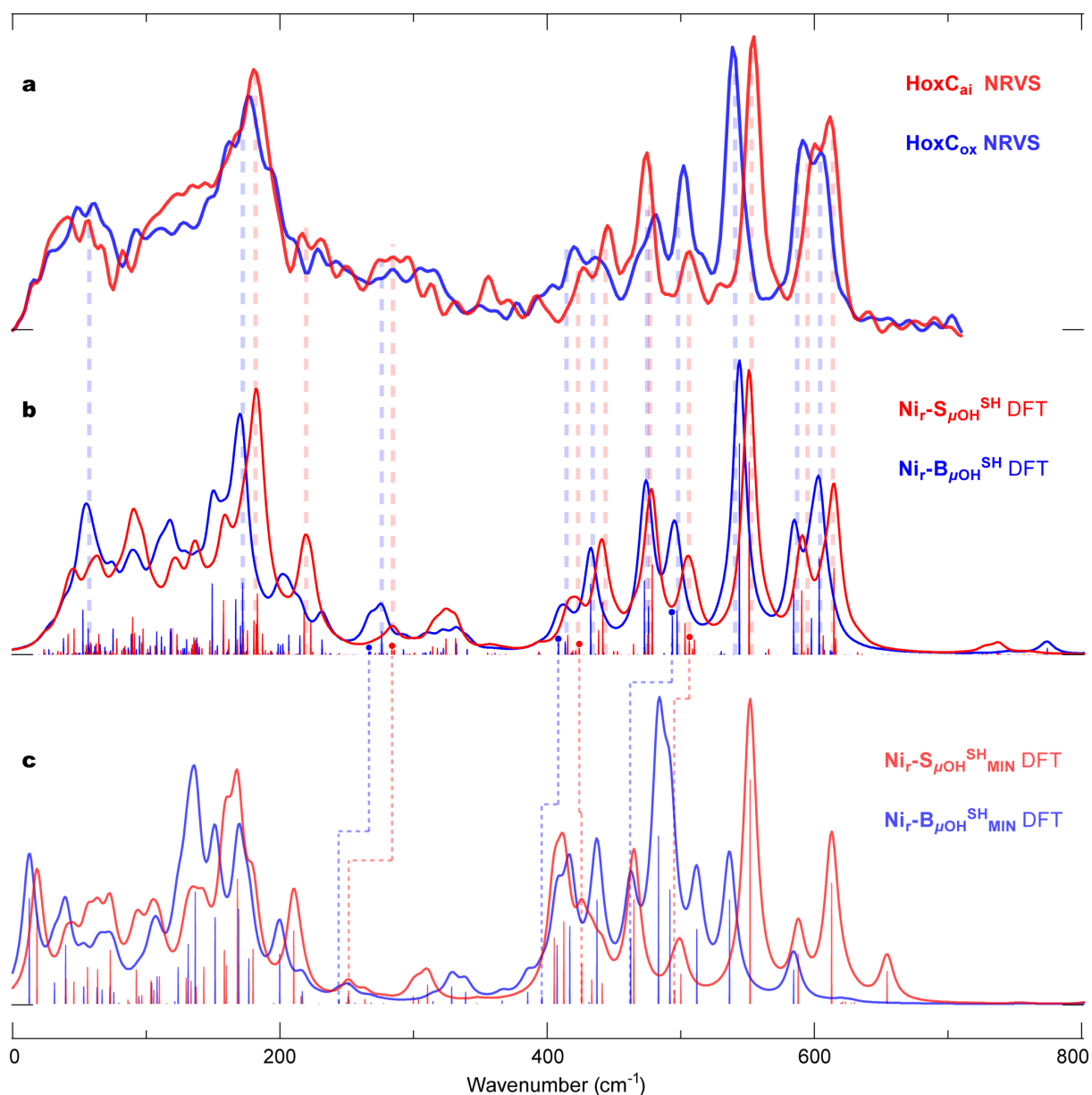


**Fig. S18** Overlay of the experimental NRVS spectra for HoxC<sub>ai</sub> (red) and HoxC<sub>ox</sub> (blue) and those derived from the corresponding DFT calculations. **a**, Experimentally observed and **b-c**, DFT-calculated <sup>57</sup>Fe-PVDOS spectra using **b**, best-fitting Ni<sub>r</sub>-S<sub>μOH</sub><sup>SH</sup> and Ni<sub>r</sub>-B<sub>μOH</sub><sup>SH</sup> and **c**, minimal Ni<sub>r</sub>-S<sub>μOH</sub><sup>SH</sup><sub>MIN</sub> and Ni<sub>r</sub>-B<sub>μOH</sub><sup>SH</sup><sub>MIN</sub> models as detailed in Materials and Methods. In (**b-c**), stick-style DFT <sup>57</sup>Fe-PVDOS data display individual mode positions and their intensities. In (**b**), the modes labeled with dots imply significant contribution from the three types of the μOH<sup>-</sup> ligand motion as depicted in **Fig. 7**. Broken lines provide either (**a to b**) tentative correlations between the bands in the experimental and best-fitting calculated spectra, or (**b to c**) matches between the principal μOH<sup>-</sup> modes in the best-fitting and minimal models.

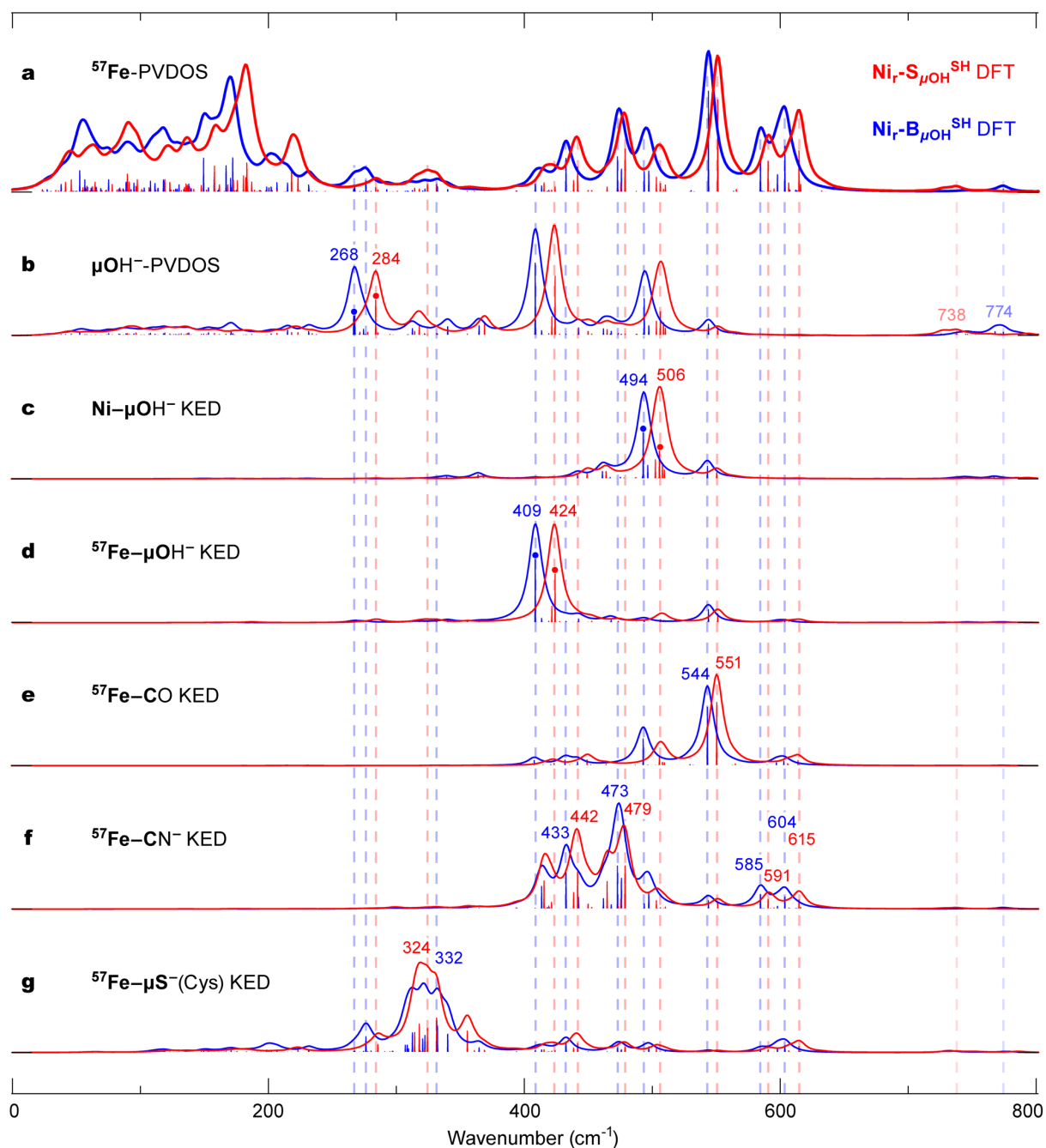
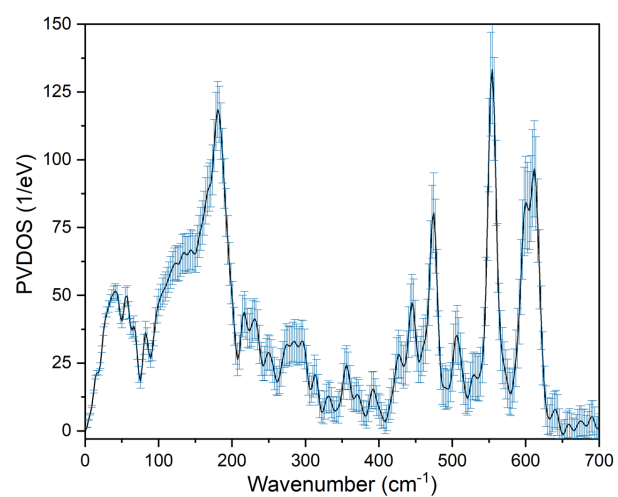
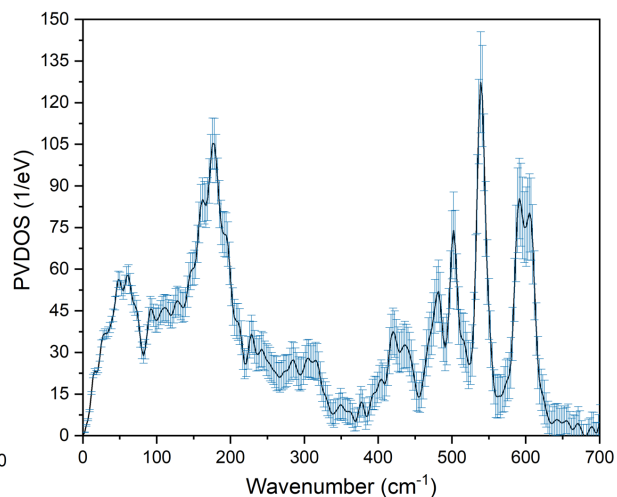


**Fig. S19** Analysis of the computed  $^{57}\text{Fe}$ -PVDOS (NRVS) spectra. **a**, Overlay of the  $^{57}\text{Fe}$ -PVDOS from the best-fit DFT models for the HoxC states, i.e.  $\text{Ni}_r\text{-S}_I$  (model  $\text{Ni}_r\text{-S}_{\mu\text{OH}}^{\text{SH}}$ , red line) and  $\text{Ni}_r\text{-B}''$  (model  $\text{Ni}_r\text{-B}_{\mu\text{OH}}^{\text{SH}}$ , blue line). **b**,  $\mu\text{O}(\text{H}^-)$ -PVDOS implying motion of the bridging hydroxyl ligand. **c-d**,  $\text{Ni}/^{57}\text{Fe}-\mu\text{O}(\text{H}^-)$  KED showing relative displacements in the metal-hydroxy bonding. **e-g**,  $^{57}\text{Fe}-\text{C}(\text{O})/\text{C}(\text{N}^-)/\mu\text{S}(\text{Cys})$  KED exposing the rest of the  $^{57}\text{Fe}$ -ligand vibrations. Vertical broken lines indicate coupling of modes of different character and provide their correlations to the  $^{57}\text{Fe}$ -PVDOS spectra. Stick-style spectra provide individual mode positions and their intensities. The modes labeled with dots (**b-d**) imply significant contribution from the  $\mu\text{OH}^-$  ligand motion, as depicted in **Fig. 7**. Animations of these modes are available in the ESI separately.

**HoxC<sub>ai</sub>**



**HoxC<sub>ox</sub>**



**RH**

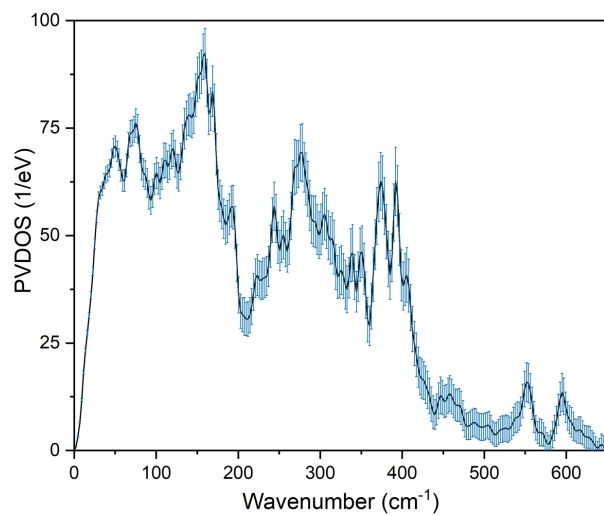


**Fig. S20** NRV spectra of HoxC<sub>ai</sub> (Ni<sub>r</sub>-S<sub>I</sub>), HoxC<sub>ox</sub> (Ni<sub>r</sub>-B'') and native RH (Ni<sub>a</sub>-S) including error bars (blue lines).

## Supplementary References

- 1 T. Buhrke, O. Lenz, N. Krauss, B. Friedrich, *J. Biol. Chem.* **2005**, *280*, 23791–23796.
- 2 G. Caserta, C. Lorent, A. Ciaccafava, M. Keck, R. Breglia, C. Greco, C. Limberg, P. Hildebrandt, S. P. Cramer, I. Zebger, O. Lenz, *Chem. Sci.*, 2020, **11**, 5453–5465.
- 3 O. Lenz, L. Lauterbach, S. Frielingsdorf, in *Methods Enzymol.*, Elsevier, 2018, 117–151.
- 4 L. B. Gee, H. Wang, S. P. Cramer, in *Methods Enzymol.*, Elsevier, 2018, 409–425.
- 5 M. Yabashi, K. Tamasaku, S. Kikuta, T. Ishikawa, *Rev. Sci. Instrum.*, 2001, **72**, 4080–4083.
- 6 W. Sturhahn, T. S. Toellner, E. E. Alp, X. Zhang, M. Ando, Y. Yoda, S. Kikuta, M. Seto, C. W. Kimball, B. Dabrowski, *Phys. Rev. Lett.*, 1995, **74**, 3832–3835.
- 7 W. Sturhahn, *Hyperfine Interact.*, 2000, **125**, 149–172.
- 8 H. Wang, Y. Yoda, S. Kamali, Z.-H. Zhou, S. P. Cramer, *J. Synchrotron Radiat.*, 2012, **19**, 257–263.
- 9 J. Fritsch, P. Scheerer, S. Frielingsdorf, S. Kroschinsky, B. Friedrich, O. Lenz, C. M. T. Spahn, *Nature*, 2011, **479**, 249–252.
- 10 C. Kortlücke, K. Horstmann, E. Schwartz, M. Rohde, R. Binsack, B. Friedrich, *J. Bacteriol.*, 1992, **174**, 6277–6289.
- 11 E. Schwartz, A. Henne, R. Cramm, T. Eitinger, B. Friedrich, G. Gottschalk, *J. Mol. Biol.*, 2003, **332**, 369–383.
- 12 *Jaguar, version 9.4, Schrodinger, Inc., New York, NY*, 2016.
- 13 M. J. Frisch, G. W. Trucks, H. B. Schlegel, G. E. Scuseria, M. A. Robb, J. R. Cheeseman, G. Scalmani, V. Barone, B. Mennucci, G. A. Petersson, H. Nakatsuji, M. Caricato, X. Li, H. P. Hratchian, A. F. Izmaylov, J. Bloino, G. Zheng, J. L. Sonnenberg, M. Hada, M. Ehara, K. Toyota, R. Fukuda, J. Hasegawa, M. Ishida, T. Nakajima, Y. Honda, O. Kitao, H. Nakai, T. Vreven, J. A. Montgomery, Jr., J. E. Peralta, F. Ogliaro, M. Bearpark, J. J. Heyd, E. Brothers, K. N. Kudin, V. N. Staroverov, R. Kobayashi, J. Normand, K. Raghavachari, A. Rendell, J. C. Burant, S. S. Iyengar, J. Tomasi, M. Cossi, N. Rega, J. M. Millam, M. Klene, J. E. Knox, J. B. Cross, V. Bakken, C. Adamo, J. Jaramillo, R. Gomperts, R. E. Stratmann, O. Yazyev, A. J. Austin, R. Cammi, C. Pomelli, J. W. Ochterski, R. L. Martin, K. Morokuma, V. G. Zakrzewski, G. A. Voth, P. Salvador, J. J. Dannenberg, S. Dapprich, A. D. Daniels, Ö. Farkas, J. B. Foresman, J. V. Ortiz, J. Cioslowski and D. J. Fox, *Gaussian 09, Revision D.01, Gaussian Inc., Wallingford CT*, 2009.
- 14 C. Adamo, V. Barone, *J. Chem. Phys.*, 1999, **110**, 6158–6170.
- 15 A. D. McLean, G. S. Chandler, *J. Chem. Phys.*, 1980, **72**, 5639–5648.
- 16 R. Krishnan, J. S. Binkley, R. Seeger, J. A. Pople, *J. Chem. Phys.*, 1980, **72**, 650–654.
- 17 J. Tomasi, B. Mennucci, R. Cammi, *Chem. Rev.*, 2005, **105**, 2999–3094.
- 18 S. Kamali, H. Wang, D. Mitra, H. Ogata, W. Lubitz, B. C. Manor, T. B. Rauchfuss, D. Byrne, V. Bonnefoy, F. E. Jenney, M. W. W. Adams, Y. Yoda, E. Alp, J. Zhao, S. P. Cramer, *Angew. Chem. Int. Ed.*, 2013, **52**, 724–728.
- 19 H. Ogata, T. Krämer, H. Wang, D. Schilter, V. Pelmeshnikov, M. van Gastel, F. Neese, T. B. Rauchfuss, L. B. Gee, A. D. Scott, Y. Yoda, Y. Tanaka, W. Lubitz, S. P. Cramer, *Nat. Commun.*, 2015, **6**, DOI 10.1038/ncomms8890.
- 20 V. Pelmeshnikov, J. A. Birrell, C. C. Pham, N. Mishra, H. Wang, C. Sommer, E. Reijerse, C. P. Richers, K. Tamasaku, Y. Yoda, T. B. Rauchfuss, W. Lubitz, S. P. Cramer, *J. Am. Chem. Soc.*, 2017, **139**, 16894–16902.
- 21 M. R. Carlson, D. L. Gray, C. P. Richers, W. Wang, P.-H. Zhao, T. B. Rauchfuss, V. Pelmeshnikov, C. C. Pham, L. B. Gee, H. Wang, S. P. Cramer, *Inorg. Chem.*, 2018, **57**, 1988–2001.
- 22 L. B. Gee, V. Pelmeshnikov, H. Wang, N. Mishra, Y.-C. Liu, Y. Yoda, K. Tamasaku, M.-H. Chiang, S. P. Cramer, *Chem. Sci.*, 2020, **11**, 5487–5493.
- 23 V. Pelmeshnikov, Y. Guo, H. Wang, S. P. Cramer, D. A. Case, *Faraday Discuss*, 2011, **148**, 409–420.
- 24 A. I. Chumakov, R. Rüffer, O. Leupold, I. Sergueev, *Struct. Chem.*, 2003, **14**, 109–119.